

---

# DUAL-SPACE POSTERIOR SAMPLING FOR BAYESIAN INFERENCE IN CONSTRAINED INVERSE PROBLEMS

---

A PREPRINT

**Ali Siahkoohi**  
Department of Computer Science  
University of Central Florida  
Orlando, FL, USA  
alisk@ucf.edu

**Kamal Aghazade**  
Institute of Geophysics  
Polish Academy of Sciences  
Warsaw, Poland  
aghazade.kamal@igf.edu.pl

**Ali Gholami**  
Institute of Geophysics  
Polish Academy of Sciences  
Warsaw, Poland  
agholami@igf.edu.pl

## ABSTRACT

Inverse problems constrained by partial differential equations are often ill-conditioned due to noisy and incomplete measured data or inherent non-uniqueness of the problem. A prominent example is full waveform inversion, which estimates Earth’s subsurface properties by fitting seismic measurements subject to the wave equation, where the ill-conditioning is inherent to noisy, band-limited, finite-aperture measured data and the presence of shadow zones. Casting the inverse problem into a Bayesian framework allows for a more comprehensive description of its solution, where instead of a single estimate, a distribution of plausible solutions—the posterior distribution—characterizes the non-uniqueness and can be sampled to quantify uncertainty. However, there is no clear procedure for translating hard physical constraints, such as the wave equation, into prior distributions that are amenable to existing sampling techniques. To address this challenge, we perform posterior sampling in the dual space using an augmented Lagrangian formulation, which translates hard constraints into penalties amenable to sampling algorithms, while ensuring their exact satisfaction. We achieve this by seamlessly integrating the alternating direction method of multipliers (ADMM) with Stein variational gradient descent (SVGD)—a particle-based sampling method—where the constraint is relaxed at each iteration and the multiplier updates progressively enforce constraint satisfaction. This enables posterior sampling in the presence of hard constraints while inheriting the favorable conditioning properties of dual-space solvers, where partial constraint relaxation allows productive updates even when the current model is far from the true solution. We validate the method on a stylized Rosenbrock conditional inference problem and on frequency-domain full waveform inversion for a Gaussian anomaly model and the Marmousi II benchmark, demonstrating well-calibrated uncertainty estimates and posterior contraction with increasing data coverage.

## 1 Introduction

Quantifying uncertainty in the solution of inverse problems is of fundamental importance in many areas of science and engineering. In geophysical applications such as seismic imaging [1], the goal is to determine the subsurface structure of the Earth from surface measurements of seismic waves. Due to the inherent ill-posedness of the problem—arising from noisy, band-limited, finite-aperture measured data and the presence of shadow zones—different models of the subsurface may explain the observed data equally well. Relying on a single estimate of the subsurface properties ignores this non-uniqueness and may lead to overconfident interpretations that fail to capture the true range of plausible solutions.

Bayesian inference provides a principled framework for characterizing this non-uniqueness by representing the solution as a probability distribution—the posterior—conditioned on the observed data [2, 3]. Sampling from the posterior yields an ensemble of models that collectively describe the range of plausible solutions and enable quantification of uncertainty in derived quantities such as confidence intervals and event probabilities. However, generating samples from the posterior in high-dimensional geophysical inverse problems remains a computational challenge [4], as each

sample requires evaluating the forward model, which for wave-based problems involves solving a partial differential equation [5, 6, 7, 8, 9].

A further challenge arises when the inverse problem is naturally posed as a constrained optimization problem—where the PDE relating model parameters to data must be satisfied as a hard constraint rather than being eliminated through direct solves. Full waveform inversion (FWI) is a paradigmatic example: the seismic wavefields are governed by the wave equation, and any model estimate must be consistent with this physics. Wavefield reconstruction methods [10, 11, 12] exploit this structure by reformulating the constrained problem using a penalty approach, in which both the model parameters and the wavefields are treated as independent variables. These methods often yield better-conditioned subproblems and improved convergence behavior compared to conventional reduced-space formulations that enforce the PDE exactly at every iteration. However, achieving accurate satisfaction of the wave equation at convergence remains challenging in purely penalty-based approaches, as large penalty parameters are typically required, which can introduce severe ill-conditioning. In contrast, augmented Lagrangian formulations [13, 14, 15] alleviate this difficulty by combining penalty terms with Lagrange multipliers, enabling progressive and precise enforcement of the PDE constraint while maintaining improved numerical stability. These dual approaches yield better conditioned subproblems and faster convergence compared to conventional reduced-space methods that enforce the PDE exactly at each iteration. However, extending these favorable properties from deterministic inversion to Bayesian inference requires a systematic procedure for translating hard PDE constraints into a sampling framework—a procedure that has remained largely unexplored. The idea of relaxing PDE constraints has proven fruitful in other fields as well—in weather forecasting, weak-constraint four-dimensional variational data assimilation [16] similarly relaxes the dynamical model constraint to improve conditioning and enable uncertainty estimation. In the context of seismic inverse problems, Fang et al. [17] relaxed the PDE constraint by introducing the wavefields as auxiliary variables and showed that the resulting extended posterior can be well-approximated by a Gaussian distribution centered at the MAP estimate. While this Gaussian approximation enables efficient sampling via the randomize-then-optimize method [18] and avoids the cost of Markov chain Monte Carlo (MCMC) [19], it has two fundamental limitations: (i) it relies on the posterior being approximately Gaussian, which precludes the characterization of multimodal or strongly non-Gaussian uncertainty that is common in complex geological settings; and (ii) it requires computing the MAP estimate and implicitly constructing the posterior covariance, which couples the sampling quality to the accuracy of a local quadratic approximation around a single mode. Recent variational approaches based on normalizing flows [20, 21] or structured variational families [22, 23] address some of these limitations but require either training neural networks or restricting the variational family to a parametric form.

In this work, we address these limitations by proposing ADMM-SVGD, a method that combines the alternating direction method of multipliers (ADMM) with Stein variational gradient descent (SVGD) to perform posterior sampling in the dual space. Like Fang et al. [17], we relax the PDE constraint and exploit the favorable conditioning of the extended formulation; however, instead of approximating the posterior as Gaussian, we represent it nonparametrically through an ensemble of interacting particles that are evolved toward the target distribution via SVGD. This particle-based representation makes no distributional assumptions and can capture multimodal posteriors, non-Gaussian tails, and complex correlation structures that a Gaussian approximation would miss. A second key difference is that, rather than fixing the penalty parameter a priori, we employ multiplier updates that progressively enforce the PDE constraint over the course of the iterations, ensuring exact constraint satisfaction at convergence without requiring a careful up-front calibration of the penalty. The augmented Lagrangian formulation admits a natural probabilistic interpretation: for fixed Lagrange multipliers, it defines an unnormalized distribution over the model that evolves as the multipliers are updated, converging to the true posterior as the constraint is progressively enforced. The resulting algorithm inherits both the favorable conditioning of dual-space solvers and the uncertainty quantification capability of particle-based sampling methods.

To validate the proposed framework, we consider three problems of increasing complexity. First, we consider conditional inference on the Rosenbrock distribution—a stylized nonlinear constrained problem where we compare ADMM-SVGD against standard SVGD (without the ADMM decomposition) to isolate the effect of the constraint splitting. Second, we apply the method to frequency-domain FWI for a Gaussian anomaly model, demonstrating well-calibrated uncertainty estimates and physically meaningful credible intervals. Third, we present results on the Marmousi II benchmark, showing posterior contraction with increasing data coverage and the emergence of multimodal uncertainty at geologically complex locations.

The remainder of the paper is organized as follows. We begin by formulating the inverse problem and its Bayesian interpretation, then review SVGD as a particle-based sampling method. We next introduce the constrained formulation and its dual-space extension via the augmented Lagrangian, derive the ADMM-SVGD algorithm, and discuss convergence considerations. Finally, we present numerical results and conclude with a discussion of the method’s strengths, limitations, and directions for future work.

## 2 Inverse problems

We are concerned with estimating an unknown model  $\mathbf{m}^* \in \mathcal{M}$ —often referred to as the unknown—from  $N_s$  noisy and indirect observed data  $\mathbf{d} = \{\mathbf{d}_i\}_{i=1}^{N_s}$  with  $\mathbf{d}_i \in \mathcal{D}$ . Here,  $\mathcal{M}$  and  $\mathcal{D}$  denote the space of unknown models and data, respectively. The physical underlying data generation process is assumed to be encoded in forward modeling operators,  $\mathcal{F}_i : \mathcal{M} \rightarrow \mathcal{D}$ , which relate the unknown model to the observed data via the forward model

$$\mathbf{d}_i = \mathcal{F}_i(\mathbf{m}^*) + \mathbf{n}_i, \quad i = 1, \dots, N_s. \quad (1)$$

In the above expression,  $\mathbf{n}_i$  is a vector of measurement noise, which might also include errors in the forward modeling operator. Solving ill-posed inverse problems is challenged by noise in the observed data, potential errors in the forward modeling operator, and the intrinsic nontrivial nullspace of the forward operator [2, 24]. These challenges can lead to non-unique solutions where different estimates of the unknown model may fit the observed data equally well.

A common approach to solving inverse problems is to formulate an optimization problem that minimizes the data misfit with an added regularization term:

$$\hat{\mathbf{m}} = \arg \min_{\mathbf{m}} \frac{1}{2} \sum_{i=1}^{N_s} \|\mathbf{d}_i - \mathcal{F}_i(\mathbf{m})\|_2^2 + \mathcal{R}(\mathbf{m}), \quad (2)$$

where  $\mathcal{R}(\mathbf{m})$  is a regularization term that incorporates prior knowledge about the model, e.g., smoothness or sparsity. While this deterministic approach yields a single point estimate  $\hat{\mathbf{m}}$ , it ignores the intrinsic variability within inverse problem solutions. Under such conditions, the use of a single model estimate increases the risk of overfitting the data. Therefore, not only does solving inverse problems require regularization, but it also calls for a statistical inference framework that allows us to characterize the variability among the solutions by quantifying the solution uncertainty.

## 3 Bayesian inference for inverse problems

To systematically quantify the uncertainty, we cast the inverse problem into a Bayesian framework [2, 25, 3]. In this framework, instead of having a single estimate of the unknown, the solution is characterized by a probability distribution over the solution space  $\mathcal{M}$  that is conditioned on data—namely the posterior distribution [26]. This conditional distribution, denoted by  $p_{\text{post}}(\mathbf{m}|\mathbf{d})$ , can according to Bayes' rule be written as follows:

$$p_{\text{post}}(\mathbf{m}|\mathbf{d}) = \frac{p_{\text{like}}(\mathbf{d}|\mathbf{m}) p_{\text{prior}}(\mathbf{m})}{p_{\text{data}}(\mathbf{d})}, \quad (3)$$

where  $p_{\text{like}}(\mathbf{d}|\mathbf{m})$  is the likelihood function, which quantifies how well the predicted data fits the observed data given the PDF of the noise distribution;  $p_{\text{prior}}(\mathbf{m})$  is the prior distribution, which encodes prior beliefs on the unknown and can also be interpreted as a regularizer for the inverse problem; and  $p_{\text{data}}(\mathbf{d})$  denotes the data PDF, which is a normalization constant that is independent of  $\mathbf{m}$ .

Under the assumption that the observed data  $\mathbf{d} = \{\mathbf{d}_i\}_{i=1}^{N_s}$  are independent conditioned on the unknown model  $\mathbf{m}$ , and assuming Gaussian noise  $\mathbf{n}_i \sim \mathcal{N}(\mathbf{0}, \sigma^2 \mathbf{I})$ , the negative log-posterior can be expressed as

$$\begin{aligned} -\log p_{\text{post}}(\mathbf{m}|\mathbf{d}) &= -\sum_{i=1}^{N_s} \log p_{\text{like}}(\mathbf{d}_i|\mathbf{m}) - \log p_{\text{prior}}(\mathbf{m}) + \log p_{\text{data}}(\mathbf{d}) \\ &= \frac{1}{2\sigma^2} \sum_{i=1}^{N_s} \|\mathbf{d}_i - \mathcal{F}_i(\mathbf{m})\|_2^2 - \log p_{\text{prior}}(\mathbf{m}) + \text{const}. \end{aligned} \quad (4)$$

In equations 3 and (4), the likelihood function  $p_{\text{like}}(\mathbf{d}_i|\mathbf{m})$  quantifies how well the predicted data (equation 1) fits the observed data given the PDF of the noise distribution. The prior distribution  $p_{\text{prior}}(\mathbf{m})$  encodes prior beliefs on the unknown quantity. Comparing equations 2 and (4), we observe that the regularization term  $\mathcal{R}(\mathbf{m})$  in the deterministic formulation corresponds to the negative log-prior  $-\log p_{\text{prior}}(\mathbf{m})$  in the Bayesian formulation—providing a probabilistic interpretation of regularization.

### 3.1 Estimation with Bayesian inference

Acquiring statistical information regarding the variability in the solutions of the inverse problem requires computing expectations with respect to the posterior distribution. For most applications, the posterior PDF itself is not directly of

interest; rather, we seek to evaluate expectations of some function  $h(\mathbf{m})$  over the posterior:

$$\mathbb{E}_{\mathbf{m} \sim p_{\text{post}}(\mathbf{m}|\mathbf{d})}[h(\mathbf{m})] = \int h(\mathbf{m}) p_{\text{post}}(\mathbf{m}|\mathbf{d}) d\mathbf{m}. \quad (5)$$

The choice of  $h$  determines what information is extracted from the posterior. For instance, setting  $h(\mathbf{m}) = \mathbf{m}$  yields the posterior mean  $\mathbb{E}[\mathbf{m}] = \int \mathbf{m} p_{\text{post}}(\mathbf{m}|\mathbf{d}) d\mathbf{m}$ , which averages over all plausible models weighted by their posterior probability. Setting  $h(\mathbf{m}) = (\mathbf{m} - \mathbb{E}[\mathbf{m}]) \circ (\mathbf{m} - \mathbb{E}[\mathbf{m}])$  provides pointwise variance estimates that characterize the spread among different models explaining the observed data. Other choices of  $h$  include indicator functions  $h(\mathbf{m}) = \mathbf{1}_{\mathcal{A}}(\mathbf{m})$ , which allow the estimation of probabilities of events  $\mathcal{A}$ —e.g., the probability that the model exceeds a threshold at a given location—a quantity of particular relevance for risk assessment in geophysical applications.

Since the posterior distribution is generally intractable and the integral in equation 5 cannot be evaluated analytically, these expectations must be approximated using Monte Carlo estimation [27, 28]. Given  $N_p$  samples  $\{\mathbf{m}^{(j)}\}_{j=1}^{N_p}$  drawn from the posterior  $p_{\text{post}}(\mathbf{m}|\mathbf{d})$ , the expectation of  $h(\mathbf{m})$  can be approximated as follows:

$$\mathbb{E}_{\mathbf{m} \sim p_{\text{post}}(\mathbf{m}|\mathbf{d})}[h(\mathbf{m})] \approx \frac{1}{N_p} \sum_{j=1}^{N_p} h(\mathbf{m}^{(j)}). \quad (6)$$

This approximation converges to the true expectation as  $N_p \rightarrow \infty$ , regardless of the dimensionality of the problem. However, obtaining samples from the posterior is itself a challenging task, particularly in high-dimensional inverse problems where each evaluation of the forward operator is computationally expensive. Before discussing how to generate these samples, we briefly review key quantities of interest that can be computed from posterior samples.

### 3.1.1 Conditional mean estimation

The conditional mean (CM), also known as the posterior mean, is obtained by setting  $h(\mathbf{m}) = \mathbf{m}$  in equation 6:

$$\mathbf{m}_{\text{CM}} = \mathbb{E}_{\mathbf{m} \sim p_{\text{post}}(\mathbf{m}|\mathbf{d})}[\mathbf{m}] \approx \frac{1}{N_p} \sum_{j=1}^{N_p} \mathbf{m}^{(j)}. \quad (7)$$

The conditional mean corresponds to the minimum-variance estimate [29] and is generally less prone to overfitting [30] compared to point estimates obtained by optimization, since it averages over the full posterior distribution rather than selecting a single mode. This was confirmed empirically for seismic imaging [31, 32, 33]. Consequently, when the data are severely contaminated by noise, the conditional mean can provide enhanced robustness. In contrast, single-mode estimates may become trapped in local minima or concentrate on narrow, noise-driven modes, whereas the conditional mean integrates over the full probability mass to yield a more stable and statistically representative solution.

### 3.1.2 Pointwise standard deviation

In its most rudimentary form, uncertainties in the model estimate can be assessed by computing the pointwise standard deviation, which expresses the spread among the different unknown models explaining the observed data. Setting  $h(\mathbf{m}) = (\mathbf{m} - \mathbf{m}_{\text{CM}}) \circ (\mathbf{m} - \mathbf{m}_{\text{CM}})$  in equation 6, this quantity can be computed via:

$$\boldsymbol{\sigma}_{\text{post}}^2 = \mathbb{E}_{\mathbf{m} \sim p_{\text{post}}(\mathbf{m}|\mathbf{d})}[(\mathbf{m} - \mathbf{m}_{\text{CM}}) \circ (\mathbf{m} - \mathbf{m}_{\text{CM}})] \approx \frac{1}{N_p} \sum_{j=1}^{N_p} (\mathbf{m}^{(j)} - \mathbf{m}_{\text{CM}}) \circ (\mathbf{m}^{(j)} - \mathbf{m}_{\text{CM}}), \quad (8)$$

where  $\circ$  denotes elementwise multiplication. The pointwise standard deviation  $\boldsymbol{\sigma}_{\text{post}}$  provides a spatially resolved measure of uncertainty: regions where the data provide strong constraints on the model will exhibit small standard deviations, whereas poorly constrained regions—such as areas with limited illumination or complex geology—will show larger values.

### 3.1.3 Confidence intervals

As described above, the pointwise standard deviation summarizes the spread among the likely estimates of the unknown. By means of this quantity, we can assign probabilities—i.e., confidence levels—to the unknown being in a certain interval. The interval is obtained by treating the pointwise posterior distribution as approximately Gaussian with mean  $\mathbf{m}_{\text{CM}}$  and standard deviation  $\boldsymbol{\sigma}_{\text{post}}$ . Given a desired confidence value—e.g., 99%—the confidence interval

is  $\mathbf{m}_{\text{CM}} \pm 2.576 \sigma_{\text{post}}$ , where 99% of samples fall between the left ( $\mathbf{m}_{\text{CM}} - 2.576 \sigma_{\text{post}}$ ) and right ( $\mathbf{m}_{\text{CM}} + 2.576 \sigma_{\text{post}}$ ) tails of the Gaussian distribution.

Computing any of these quantities requires drawing samples from the posterior. In the next section, we describe SVGD, a particle-based method that generates approximate posterior samples by evolving an ensemble of models toward the target distribution.

## 4 Stein variational gradient descent

SVGD is a particle-based deterministic method for approximate Bayesian inference [34]. Rather than sampling sequentially as in MCMC methods [19], SVGD evolves an ensemble of  $N_p$  particles  $\{\mathbf{m}^{(j)}\}_{j=1}^{N_p}$  to approximate the target posterior distribution. This approach offers several practical advantages over MCMC for geophysical inverse problems [e.g., 35, 22, 36]: (i) the particles can be evolved in parallel; (ii) there is no burn-in period; and (iii) the method is deterministic given the initial particle positions.

The particles are updated iteratively according to:

$$\mathbf{m}^{(j)} \leftarrow \mathbf{m}^{(j)} + \eta \phi^*(\mathbf{m}^{(j)}), \quad (9)$$

where  $\eta$  is the step size and the optimal perturbation direction is:

$$\phi^*(\mathbf{m}^{(j)}) = \frac{1}{N_p} \sum_{i=1}^{N_p} \left[ K(\mathbf{m}^{(i)}, \mathbf{m}^{(j)}) \nabla_{\mathbf{m}^{(i)}} \log p_{\text{post}}(\mathbf{m}^{(i)} | \mathbf{d}) + \nabla_{\mathbf{m}^{(i)}} K(\mathbf{m}^{(i)}, \mathbf{m}^{(j)}) \right]. \quad (10)$$

Here,  $K(\cdot, \cdot)$  is a positive definite kernel, commonly chosen as the radial basis function (RBF) kernel:

$$K(\mathbf{m}, \mathbf{m}') = \exp\left(-\frac{\|\mathbf{m} - \mathbf{m}'\|^2}{2h^2}\right), \quad (11)$$

with bandwidth  $h$  typically set using the median heuristic [34]:

$$h = \frac{\text{median}(\{\|\mathbf{m}^{(i)} - \mathbf{m}^{(j)}\|_2 : 1 \leq i < j \leq N_p\})}{\sqrt{2 \log N_p}}, \quad (12)$$

where the median is taken over all  $N_p(N_p - 1)/2$  pairwise Euclidean distances between distinct particles. The update in equation 10 consists of two terms that together balance exploration and exploitation. The first term drives particles toward regions of high posterior probability by performing gradient ascent on the log-posterior, weighted by the kernel—this term is responsible for fitting the observed data and respecting the prior. The second term acts as a repulsive force between nearby particles, maintaining diversity among the ensemble and preventing all particles from collapsing to a single mode of the posterior. This repulsion is essential for uncertainty quantification, as it ensures that the particle ensemble captures the spread of the posterior rather than concentrating around a single point estimate. The bandwidth  $h$  of the kernel controls the range of interaction between particles: a larger bandwidth encourages global exploration, while a smaller bandwidth allows particles to resolve finer structure in the posterior. The median heuristic provides an adaptive choice that scales with the current spread of the ensemble.

SVGD requires only the gradient of the log-posterior,  $\nabla_{\mathbf{m}} \log p_{\text{post}}(\mathbf{m} | \mathbf{d})$ , which can be computed using adjoint methods in many geophysical applications [37, 1]. Additionally, the particle-based nature of SVGD makes it particularly well-suited for integration with iterative optimization schemes such as the alternating direction method of multipliers (ADMM). As we demonstrate below, SVGD can be seamlessly combined with dual-space methods to handle constrained inverse problems, where the physics constraints are incorporated through a Lagrangian formulation rather than being enforced exactly at each iteration. The algorithm is summarized in Algorithm 1.

**Algorithm 1** Stein Variational Gradient Descent (SVGD)

---

```

1: Input: Target posterior  $p_{\text{post}}(\mathbf{m}|\mathbf{d})$ , number of particles  $N_p$ , step size  $\eta$ 
2: Initialize: Sample  $\mathbf{m}^{(j)} \sim p_{\text{prior}}(\mathbf{m})$  for  $j = 1, \dots, N_p$ 
3: while not converged do
4:   for  $j = 1, \dots, N_p$  do
5:     Compute gradient:  $\mathbf{g}^{(j)} = \nabla_{\mathbf{m}} \log p_{\text{post}}(\mathbf{m}^{(j)}|\mathbf{d})$ 
6:   end for
7:   Compute kernel bandwidth  $h$  via equation 12
8:   for  $j = 1, \dots, N_p$  do
9:      $\phi^{(j)} \leftarrow \frac{1}{N_p} \sum_{i=1}^{N_p} [K(\mathbf{m}^{(i)}, \mathbf{m}^{(j)})\mathbf{g}^{(i)} + \nabla_{\mathbf{m}^{(i)}} K(\mathbf{m}^{(i)}, \mathbf{m}^{(j)})]$ 
10:  end for
11:  for  $j = 1, \dots, N_p$  do
12:     $\mathbf{m}^{(j)} \leftarrow \mathbf{m}^{(j)} + \eta \phi^{(j)}$ 
13:  end for
14: end while
15: Output: Posterior samples  $\{\mathbf{m}^{(j)}\}_{j=1}^{N_p}$ 

```

---

## 5 Constrained inverse problems

In many inverse problems, the forward operator  $\mathcal{F}_i$  is not given in closed form but is instead implicitly defined through a physical constraint that must be solved numerically. FWI is a prominent example [38, 1]: the forward model requires solving the wave equation for each source experiment. Recognizing this structure, the inverse problem can be cast as a constrained optimization problem [39]. For a medium characterized by the squared slowness  $\mathbf{m} \in \mathbb{R}^N$ , the seismic wavefields  $\mathbf{u}_i \in \mathbb{C}^N$ , and observed data  $\mathbf{d}_i \in \mathbb{C}^{N_r}$ , the constrained formulation reads:

$$\underset{\mathbf{m}, \{\mathbf{u}_i\}_{i=1}^{N_s}}{\text{minimize}} \quad \frac{1}{2\sigma^2} \sum_{i=1}^{N_s} \|\mathbf{P}\mathbf{u}_i - \mathbf{d}_i\|_2^2 \quad \text{subject to} \quad \mathbf{A}(\mathbf{m})\mathbf{u}_i = \mathbf{b}_i, \quad i = 1, \dots, N_s. \quad (13)$$

Here, the objective measures the weighted data misfit between observed data  $\mathbf{d}_i$  and predicted data at receiver locations, where  $\mathbf{P} \in \mathbb{R}^{N_r \times N}$  is the receiver sampling operator ( $N_r \ll N$ ) and  $\sigma^2$  is the noise variance. The constraints  $\mathbf{A}(\mathbf{m})\mathbf{u}_i = \mathbf{b}_i$  encode the wave physics:  $\mathbf{A}(\mathbf{m}) = (\omega^2 \text{diag}(\mathbf{m}) + \Delta) \in \mathbb{C}^{N \times N}$  is the Helmholtz operator at angular frequency  $\omega$ ,  $\Delta$  is the Laplacian with appropriate boundary conditions, and  $\mathbf{b}_i \in \mathbb{C}^N$  is the source term for the  $i$ -th experiment. By eliminating  $\mathbf{u}_i$  via the constraint, the forward operator from equation 1 takes the form  $\mathcal{F}_i(\mathbf{m}) = \mathbf{P}\mathbf{A}(\mathbf{m})^{-1}\mathbf{b}_i$ , which recovers the standard reduced formulation presented in equation 2.

Viewing FWI as a constrained problem—rather than eliminating the constraint upfront—opens the door to solvers that treat both the model  $\mathbf{m}$  and the wavefields  $\{\mathbf{u}_i\}_{i=1}^{N_s}$  as independent variables. In this formulation, the wave equation need not be satisfied exactly at each iteration; instead, it is progressively enforced over the course of the iterations. This relaxation is advantageous for two reasons. First, it breaks the tight coupling between model and wavefield variables, significantly reducing the ill-conditioning that plagues the reduced-space approach where  $\mathbf{u}_i = \mathbf{A}(\mathbf{m})^{-1}\mathbf{b}_i$  is enforced at every step. Second, it enables iterative solvers—such as the ADMM [13]—that approximately satisfy the constraint in early iterations and progressively dial in accuracy, yielding better conditioned subproblems and faster overall convergence.

### 5.1 Challenges for Bayesian inference in constrained inverse problems

While the constrained formulation 13 offers clear benefits for deterministic inversion, the core challenge is that it is unclear how to systematically incorporate such constraints into a Bayesian inference framework. The standard Bayesian approach of equation 4 operates exclusively in the reduced space, evaluating  $\mathcal{F}_i(\mathbf{m}) = \mathbf{P}\mathbf{A}(\mathbf{m})^{-1}\mathbf{b}_i$  and implicitly enforcing exact constraint satisfaction at every posterior evaluation. Critically, this reduced-space formulation produces a posterior distribution that is highly nonlinear in the model parameters  $\mathbf{m}$ , because the forward map  $\mathcal{F}_i$  inherits the full nonlinearity of the PDE solve. As demonstrated by Fang et al. [17], this nonlinearity manifests as spurious local modes in the negative log-posterior landscape—modes that do not correspond to physically meaningful solutions but arise as artifacts of the tight coupling between model and wavefields in the reduced formulation. These spurious modes severely hinder both optimization (which may converge to a local minimum rather than the global MAP estimate) and sampling (which requires either traversing high-energy barriers between modes or running impractically long Markov chains).

Two common strategies for handling the constraint each come with significant drawbacks. The first is to relax the hard constraint into a soft penalty [10, 11], replacing the wave equation by an additive term  $\frac{\mu}{2} \|\mathbf{A}(\mathbf{m})\mathbf{u}_i - \mathbf{b}_i\|_2^2$  in the objective. As shown by Fang et al. [17], for an appropriate choice of the penalty parameter, the resulting extended posterior has fewer modes than the reduced formulation, because the relaxation breaks the tight nonlinear coupling between  $\mathbf{m}$  and the data. However, the accuracy of the solution depends critically on the penalty parameter  $\mu$ : too small, and the wave equation is not sufficiently enforced; too large, and the problem recovers the multimodal landscape of the reduced formulation. Crucially, for the posterior samples to be physically meaningful, the constraint must eventually be satisfied to high accuracy—a soft penalty alone offers no guarantee of this. The second strategy is reparameterization: eliminating the wavefields by substituting  $\mathbf{u}_i = \mathbf{A}(\mathbf{m})^{-1}\mathbf{b}_i$ , which implicitly satisfies the constraint. This is the reduced-space approach, and while it removes the need to handle the constraint explicitly, it tightly couples  $\mathbf{m}$  and  $\mathbf{u}_i$ , producing the highly multimodal posterior described above and making sampling significantly more challenging.

To reap the benefits of the full-space formulation—where the constraint is only approximately satisfied in early iterations, with accuracy dialed in progressively—while avoiding both the multimodality of the reduced formulation and the limitations of a fixed-penalty approach, we propose a dual-space approach based on the augmented Lagrangian. By introducing Lagrange multipliers (dual variables), we derive a formulation that naturally balances data fidelity, prior information, and constraint enforcement, enabling posterior sampling without requiring exact constraint satisfaction at each step. The key advantage over a fixed penalty is that the multiplier updates provide a principled mechanism for progressively tightening the constraint, so that the extended posterior converges to the true posterior regardless of the initial penalty choice.

## 6 Dual-space Bayesian inference for constrained inverse problems

To enable flexible Bayesian inference for the constrained problem (equation 13), we introduce a dual-space formulation based on the augmented Lagrangian method. This approach offers several advantages that translate naturally to the Bayesian setting.

### 6.1 Lagrangian formulation

The well-established method of Lagrange multipliers can be used to solve the constrained inverse problem presented in equation 13. This approach involves optimization of the Lagrangian function, defined as follows:

$$\mathcal{L}(\mathbf{m}, \mathbf{u}, \mathbf{v}) = \frac{1}{2\sigma^2} \sum_{i=1}^{N_s} \|\mathbf{P}\mathbf{u}_i - \mathbf{d}_i\|_2^2 + \sum_{i=1}^{N_s} \langle \mathbf{v}_i, \mathbf{A}(\mathbf{m})\mathbf{u}_i - \mathbf{b}_i \rangle, \quad (14)$$

In the above expression,  $\mathbf{v}_i \in \mathbb{C}^N$  denotes the Lagrange multipliers—i.e., dual variables—associated with the wave equation constraint for source  $i$ , and  $\langle \cdot, \cdot \rangle$  denotes the inner product. The Lagrange multipliers play the role of adjoint wavefields: they encode the sensitivity of the objective to violations of the wave equation and provide the mechanism through which the physics constraints influence the optimization. The optimum point of the Lagrangian is a saddle point which attains a minimum over the primal variables  $\mathbf{m}$  and  $\mathbf{u}_i$  and a maximum over the dual variables  $\mathbf{v}_i$ .

### 6.2 Augmented Lagrangian formulation

While the standard Lagrangian provides the correct solution at its saddle point, it does not penalize constraint violations during the iterative process, which can lead to ill-conditioning. The augmented Lagrangian method [13, 14, 40] addresses this by adding a quadratic penalty term that penalizes deviations from the wave equation:

$$\mathcal{L}_\mu(\mathbf{m}, \mathbf{u}, \mathbf{v}) = \frac{1}{2\sigma^2} \sum_{i=1}^{N_s} \|\mathbf{P}\mathbf{u}_i - \mathbf{d}_i\|_2^2 + \sum_{i=1}^{N_s} \langle \mathbf{v}_i, \mathbf{A}(\mathbf{m})\mathbf{u}_i - \mathbf{b}_i \rangle + \frac{\mu}{2} \sum_{i=1}^{N_s} \|\mathbf{A}(\mathbf{m})\mathbf{u}_i - \mathbf{b}_i\|_2^2, \quad (15)$$

where  $\mu > 0$  is the penalty parameter. The solution to the constrained problem 13 corresponds to a saddle point:

$$\underset{\mathbf{m}, \mathbf{u}}{\text{minimize}} \underset{\mathbf{v}}{\text{maximize}} \mathcal{L}_\mu(\mathbf{m}, \mathbf{u}, \mathbf{v}). \quad (16)$$

By introducing the scaled multiplier  $\boldsymbol{\varepsilon}_i = \frac{1}{\mu}\mathbf{v}_i$ —which absorbs the penalty parameter into the dual variable—the augmented Lagrangian can be rewritten in a more compact and computationally convenient form:

$$\mathcal{L}_\mu(\mathbf{m}, \mathbf{u}, \boldsymbol{\varepsilon}) = \frac{1}{2\sigma^2} \sum_{i=1}^{N_s} \|\mathbf{P}\mathbf{u}_i - \mathbf{d}_i\|_2^2 + \frac{\mu}{2} \sum_{i=1}^{N_s} \|\mathbf{A}(\mathbf{m})\mathbf{u}_i - \mathbf{b}_i + \boldsymbol{\varepsilon}_i\|_2^2 - \frac{\mu}{2} \sum_{i=1}^{N_s} \|\boldsymbol{\varepsilon}_i\|_2^2. \quad (17)$$

This formulation provides several benefits over the reduced-space approach: (i) the quadratic penalty term adds curvature to the objective, significantly improving the convergence behavior compared to the standard Lagrangian or the reduced-space approach; (ii) the problem decomposes into subproblems over the model, wavefields, and multipliers that can be solved iteratively via the ADMM [13, 40], avoiding the need for simultaneous updates of all variables; and (iii) the wave equation constraint does not need to be satisfied exactly at each iteration—only in the limit of convergence—which allows the algorithm to take productive steps even when the current model is far from the true solution.

### 6.3 Probabilistic interpretation

A central advantage of the augmented Lagrangian formulation is that it admits a natural probabilistic interpretation, which provides the bridge between constrained optimization and Bayesian inference. The idea is to treat the augmented Lagrangian as a negative log-density—for fixed auxiliary variables  $\mathbf{u}$  and multipliers  $\boldsymbol{\varepsilon}$ , the augmented Lagrangian defines an unnormalized probability distribution over  $\mathbf{m}$ :

$$p(\mathbf{m}|\mathbf{d}, \boldsymbol{\varepsilon}) \propto \exp(-\mathcal{L}_\mu(\mathbf{m}, \mathbf{u}, \boldsymbol{\varepsilon})) \cdot p_{\text{prior}}(\mathbf{m}), \quad (18)$$

where  $\mathbf{u}$  is obtained by solving the optimality conditions of the augmented Lagrangian given  $(\mathbf{m}, \boldsymbol{\varepsilon})$ . Crucially, this distribution over  $\mathbf{m}$  depends on the current multipliers  $\boldsymbol{\varepsilon}$ , and therefore evolves as these are updated. Denoting the multipliers at iteration  $k$  by  $[\boldsymbol{\varepsilon}]_k$ , the algorithm generates a sequence of target distributions

$$p_k(\mathbf{m}|\mathbf{d}) := p(\mathbf{m}|\mathbf{d}, [\boldsymbol{\varepsilon}]_k) \xrightarrow{k \rightarrow \infty} p_{\text{post}}(\mathbf{m}|\mathbf{d}). \quad (19)$$

At each iteration, the SVGD update transports the model particles toward approximate samples from  $p_k(\mathbf{m}|\mathbf{d})$ ; the auxiliary variables and multipliers are then updated, refining the target distribution for the next iteration. As the multipliers converge to their optimal values and the constraint residuals vanish, the evolving distribution  $p_k$  converges to the true posterior, and the model particles become approximate samples from it. We provide justification for why this convergence can be expected in practice following the algorithm description.

Taking the negative logarithm and using equation 15, we obtain

$$\begin{aligned} -\log p(\mathbf{m}|\mathbf{d}, \mathbf{v}) &= \mathcal{L}_\mu(\mathbf{m}, \mathbf{u}, \mathbf{v}) - \log p_{\text{prior}}(\mathbf{m}) + \text{const} \\ &= \underbrace{\frac{1}{2\sigma^2} \sum_{i=1}^{N_s} \|\mathbf{P}\mathbf{u}_i - \mathbf{d}_i\|_2^2}_{\text{data fidelity term}} + \underbrace{\sum_{i=1}^{N_s} \text{Re}\langle \mathbf{v}_i, \mathbf{A}(\mathbf{m})\mathbf{u}_i - \mathbf{b}_i \rangle}_{\text{multiplier term}} \\ &\quad + \underbrace{\frac{\mu}{2} \sum_{i=1}^{N_s} \|\mathbf{A}(\mathbf{m})\mathbf{u}_i - \mathbf{b}_i\|_2^2}_{\text{penalty term}} - \underbrace{\log p_{\text{prior}}(\mathbf{m})}_{\text{log-prior}}. \end{aligned} \quad (20)$$

Each term in the above expression plays a distinct role. The data fidelity term measures the misfit between the predicted wavefield at receiver locations and the observed data—under the Gaussian noise assumption, this term corresponds to the negative log-likelihood  $-\log p_{\text{like}}(\mathbf{d}|\mathbf{m})$ . The linear multiplier term encodes accumulated information from the Lagrange multipliers—i.e., the adjoint wavefields—that steer the solution toward satisfying the wave equation; this term evolves over iterations as the multipliers are updated. The penalty term penalizes violations of the wave equation  $\mathbf{A}(\mathbf{m})\mathbf{u} = \mathbf{b}$  through a quadratic term scaled by the penalty parameter  $\mu$ , where larger values of  $\mu$  enforce the constraint more strictly but may lead to ill-conditioning. Finally, the negative log-prior incorporates prior knowledge about the model, e.g., smoothness or spatial correlation, regularizing the solution in a manner analogous to the deterministic setting [see 41, equation 2].

The key insight is that rather than enforcing the wave equation exactly—which couples  $\mathbf{m}$  and  $\mathbf{u}$  tightly—the augmented Lagrangian relaxes this coupling. By employing a moderate penalty parameter  $\mu$ , the resulting subproblems remain better conditioned, while the iterative multiplier updates progressively enforce the PDE constraint and steer the evolving distribution toward the true posterior. In early iterations, the auxiliary variables and multipliers are far from their optimal values, and the distribution in equation 18 only coarsely approximates the true posterior; nevertheless, sampling from this approximate distribution still provides useful gradient information that moves the model particles in a productive direction. As the iterations progress and the constraint is increasingly enforced, the distribution sharpens and converges to the true posterior, so that the final particle positions represent approximate posterior samples that satisfy the physics constraints.

## 6.4 ADMM-SVGD algorithm

Having established the probabilistic interpretation of the augmented Lagrangian, we now combine ADMM with SVGD to sample from the posterior distribution in the dual space. The integration of these two methods is natural: ADMM provides the iterative structure for handling the physics constraints through dual variables, while SVGD enables uncertainty quantification by evolving an ensemble of particles toward the posterior distribution. A key advantage of this combination is that the gradient of the log-posterior required by SVGD (equation 10) can be obtained directly from the dual iteration equations, avoiding the need for explicit adjoint solves that would otherwise be required in the reduced-space formulation. Each particle independently solves its own set of auxiliary equations, making the per-particle computations embarrassingly parallel, while the SVGD kernel interactions across particles maintain diversity and prevent mode collapse.

The algorithm maintains an ensemble of  $N_p$  model particles  $\{\mathbf{m}^{(j)}\}_{j=1}^{N_p}$ , each with its own set of auxiliary wavefields  $\mathbf{u}_i^{(j)}$  and scaled multipliers  $\boldsymbol{\varepsilon}_i^{(j)}$  that are updated iteratively. The model particles are the primary unknowns—they represent the posterior samples at convergence—while the auxiliary variables serve as per-particle bookkeeping that drives each particle toward constraint satisfaction. The algorithm iterates through the following steps.

**Step 1: Auxiliary variables.** For each particle  $j$ , compute auxiliary variables by solving the dual iteration equations. The matrix  $\mathbf{S}^{(j)} = \mathbf{P}\mathbf{A}(\mathbf{m}^{(j)})^{-1}$  represents the forward modeling operator for the current model estimate of particle  $j$ , mapping sources to predicted data at receiver locations. The data residual  $\delta\mathbf{d}_i^{(j)} = \mathbf{d}_i - \mathbf{S}^{(j)}\mathbf{b}_i$  quantifies the misfit between observed and predicted data. The adjoint wavefields  $\boldsymbol{\lambda}_i^{(j)}$  are obtained from the optimality condition of the wavefield subproblem—which balances the data fidelity (scaled by  $1/\sigma^2$ ) against the constraint penalty (scaled by  $\mu$ ):

$$\boldsymbol{\lambda}_i^{(j)} = \mathbf{S}^{(j)H}(\mathbf{S}^{(j)}\mathbf{S}^{(j)H} + \mu\sigma^2\mathbf{I})^{-1}(\delta\mathbf{d}_i^{(j)} + \mathbf{S}^{(j)}\boldsymbol{\varepsilon}_i^{(j)}), \quad (21)$$

$$\mathbf{u}_i^{(j)} = \mathbf{A}(\mathbf{m}^{(j)})^{-1}(\mathbf{b}_i + \boldsymbol{\lambda}_i^{(j)} - \boldsymbol{\varepsilon}_i^{(j)}). \quad (22)$$

The quantity  $\mu\sigma^2$  controls the balance between data fitting and constraint enforcement: small values prioritize the data, while large values prioritize the wave equation constraint. In the limit  $\sigma^2 \rightarrow 0$  (exact data), the system reduces to  $\mathbf{S}^{(j)}\boldsymbol{\lambda}_i^{(j)} = \delta\mathbf{d}_i^{(j)} + \mathbf{S}^{(j)}\boldsymbol{\varepsilon}_i^{(j)}$ , recovering exact data fitting at receiver locations. In this work, we adopt the residual-whiteness principle to adaptively determine the parameter  $\mu\sigma^2$  at each iteration [see 42].

**Step 2: Gradient computation.** Once the auxiliary variables are available, the gradient of the log-posterior with respect to  $\mathbf{m}^{(j)}$  can be computed. This gradient naturally decomposes into a likelihood term—derived from the data misfit and constraint penalty—and a prior term:

$$\mathbf{g}_m^{(j)} = \mathbf{g}_{\text{like}}^{(j)} + \mathbf{g}_{\text{prior}}^{(j)}. \quad (23)$$

The likelihood gradient is computed from the dual iteration as:

$$\mathbf{g}_{\text{like}}^{(j)} = -\frac{1}{\omega^2} \frac{\sum_{i=1}^{N_s} \text{Re} \left( (\mathbf{u}_i^{(j)})^* \circ \boldsymbol{\lambda}_i^{(j)} \right)}{\sum_{i=1}^{N_s} (\mathbf{u}_i^{(j)})^* \circ \mathbf{u}_i^{(j)}}, \quad (24)$$

In the above expression,  $\circ$  denotes elementwise multiplication and  $*$  denotes complex conjugate. This expression has the familiar structure of a zero-lag cross-correlation between the forward wavefield  $\mathbf{u}_i^{(j)}$  and the adjoint wavefield  $\boldsymbol{\lambda}_i^{(j)}$ , analogous to the gradient computation in adjoint-state methods for FWI [37]. The prior gradient depends on the choice of prior:

$$\mathbf{g}_{\text{prior}}^{(j)} = \nabla_{\mathbf{m}} \log p_{\text{prior}}(\mathbf{m}^{(j)}). \quad (25)$$

**Step 3: SVGD update for model.** With the gradients computed, the model particles are updated using the SVGD perturbation (equation 10), which combines the gradient-driven term—that moves particles toward high-probability regions—with the repulsive kernel term that maintains ensemble diversity:

$$\mathbf{m}^{(j)} \leftarrow \mathbf{m}^{(j)} + \eta_m \boldsymbol{\phi}_m^{(j)}, \quad (26)$$

where

$$\boldsymbol{\phi}_m^{(j)} = \frac{1}{N_p} \sum_{i=1}^{N_p} \left[ K(\mathbf{m}^{(i)}, \mathbf{m}^{(j)}) \mathbf{g}_m^{(i)} + \nabla_{\mathbf{m}^{(i)}} K(\mathbf{m}^{(i)}, \mathbf{m}^{(j)}) \right]. \quad (27)$$

**Step 4: Multiplier update.** Finally, the scaled Lagrange multipliers are updated by accumulating the wave equation residual. This dual ascent step is the mechanism by which the algorithm progressively enforces the physics constraint—if the wave equation is not satisfied for a given particle, the multiplier grows, increasing the penalty on constraint violations in subsequent iterations:

$$\varepsilon_i^{(j)} \leftarrow \varepsilon_i^{(j)} + \mathbf{A}(\mathbf{m}^{(j)})\mathbf{u}_i^{(j)} - \mathbf{b}_i. \quad (28)$$

The algorithm is summarized in Algorithm 2. A Julia implementation of the sampler, along with code to reproduce the Rosenbrock example, is available on [GitHub](#).

---

**Algorithm 2** ADMM-SVGD for constrained Bayesian inverse problems

---

- 1: **Input:** Data  $\{\mathbf{d}_i\}_{i=1}^{N_s}$ , sources  $\{\mathbf{b}_i\}_{i=1}^{N_s}$ , prior  $p_{\text{prior}}(\mathbf{m})$ , noise level  $\sigma$ , penalty  $\mu$ , particles  $N_p$ , step size  $\eta_m$
  - 2: **Initialize:** Sample  $\mathbf{m}^{(j)} \sim p_{\text{prior}}(\mathbf{m})$ , set  $\varepsilon_i^{(j)} = \mathbf{0}$  for  $j = 1, \dots, N_p$ ,  $i = 1, \dots, N_s$
  - 3: **while** not converged **do**
  - 4:   **for**  $j = 1, \dots, N_p$  **do** ▷ Embarrassingly parallel
  - 5:     Compute  $\mathbf{S}^{(j)} = \mathbf{P}\mathbf{A}(\mathbf{m}^{(j)})^{-1}$ ,  $\delta\mathbf{d}_i^{(j)} = \mathbf{d}_i - \mathbf{S}^{(j)}\mathbf{b}_i$  for all  $i$
  - 6:     Solve for  $\lambda_i^{(j)}$  for all  $i$  via equation 21
  - 7:     Solve for  $\mathbf{u}_i^{(j)}$  for all  $i$  via equation 22
  - 8:     Compute  $\mathbf{g}_{\text{like}}^{(j)}$  via equation 24
  - 9:     Compute  $\mathbf{g}_m^{(j)} = \mathbf{g}_{\text{like}}^{(j)} + \nabla_{\mathbf{m}} \log p_{\text{prior}}(\mathbf{m}^{(j)})$
  - 10:   **end for**
  - 11:   Compute kernel bandwidth  $h$  via equation 12
  - 12:   **for**  $j = 1, \dots, N_p$  **do** ▷ Embarrassingly parallel
  - 13:     Compute  $\phi_m^{(j)}$  via equation 27
  - 14:   **end for**
  - 15:   **for**  $j = 1, \dots, N_p$  **do** ▷ Embarrassingly parallel
  - 16:     Update  $\mathbf{m}^{(j)} \leftarrow \mathbf{m}^{(j)} + \eta_m \phi_m^{(j)}$
  - 17:     Update  $\varepsilon_i^{(j)} \leftarrow \varepsilon_i^{(j)} + \mathbf{A}(\mathbf{m}^{(j)})\mathbf{u}_i^{(j)} - \mathbf{b}_i$  for all  $i$
  - 18:   **end for**
  - 19: **end while**
  - 20: **Output:** Posterior samples  $\{\mathbf{m}^{(j)}\}_{j=1}^{N_p}$  approximating  $p_{\text{post}}(\mathbf{m}|\mathbf{d})$
- 

The computational cost per iteration is dominated by the auxiliary variable solves in Step 1, each of which requires applying the inverse of the Helmholtz operator  $\mathbf{A}(\mathbf{m}^{(j)})^{-1}$ . Crucially, these solves are embarrassingly parallel across both particles and sources, making the algorithm well-suited for modern parallel computing architectures. The multiplier update (Step 4) and the SVGD perturbation computation (Step 3) are also independent across particles. This structure is akin to consensus optimization [43]: each particle acts as an independent worker that solves its own auxiliary equations and accumulates its own multiplier updates, while the SVGD kernel step acts as a coordination mechanism that aggregates information across the ensemble to maintain diversity and prevent mode collapse. The only inter-particle communication occurs through the kernel evaluations in Step 3, which require access to all particle positions and gradients but can themselves be computed in parallel. At convergence, the constraint residual  $\|\mathbf{A}(\mathbf{m}^{(j)})\mathbf{u}_i^{(j)} - \mathbf{b}_i\|$  vanishes for each particle, ensuring that the posterior samples satisfy the physics constraints while the SVGD kernel interactions maintain the diversity needed for reliable uncertainty quantification.

## 6.5 Convergence considerations

A natural question is whether the evolving distribution  $p_k(\mathbf{m}|\mathbf{d})$  converges to the true posterior. A complete proof for the general nonconvex setting remains open, but several lines of evidence provide strong support.

First, ADMM is known to tolerate approximate subproblem solves: Tapia [44] and Miele et al. [45] established early on that multiplier methods converge even when the inner minimization is performed inexactly, and Eckstein and Bertsekas [46] proved that convergence is preserved as long as the approximation errors decrease over iterations. Boyd et al. [47] showed that larger errors are permissible in early iterations when the iterates are far from the solution. In our setting, this is naturally satisfied through warm-starting—as the multipliers stabilize,  $p_k$  changes slowly between iterations, so the particles from the previous step already approximate the current target well. Second, for nonconvex objectives—typical in geophysical applications—Hong et al. [48] and Wang et al. [49] established that ADMM converges to

stationary points provided  $\mu$  is sufficiently large. Third, Vono et al. [50] and Vono et al. [51] proved that ADMM-type splitting is compatible with sampling (not just optimization), achieving dimension-free convergence rates for a split Gibbs sampler. Their analysis reveals a tradeoff: larger  $\mu$  enforces the constraint faster but introduces temporary bias, while smaller  $\mu$  reduces bias but slows convergence. Finally, Korba et al. [52] showed that the SVGD approximation error decreases as  $O(1/T)$  after  $T$  steps, with an additional  $O(1/\sqrt{N_p})$  term from using finitely many particles.

In practice, care should be taken with the choice of  $\mu$  [47] and with using enough particles to avoid underestimating the posterior spread [34].

## 7 Numerical examples

The proposed ADMM-SVGd framework is validated on two classes of problems. First, we consider conditional inference on the Rosenbrock distribution as a stylized example that demonstrates the method’s ability to perform Bayesian inference under nonlinear constraints. Second, we apply the method to full waveform inversion, where the wave equation constraint is enforced through the dual-space formulation. For the FWI experiments, we present results on a Gaussian anomaly model and on the Marmousi II model, progressively increasing the complexity of the subsurface structure.

### 7.1 Conditional inference on the Rosenbrock distribution

As a controlled demonstration of ADMM-SVGd for conditional inference, we consider sampling from the posterior distribution  $p(\mathbf{x}|\mathbf{y})$  where the prior  $p(\mathbf{x})$  follows the Rosenbrock distribution—a banana-shaped density defined by  $p(\mathbf{x}) \propto \exp(-a(x_1 - \mu_0)^2 - (x_2 - x_1^2)^2)$ —and the observations are generated as  $\mathbf{y} = \mathbf{x} + \boldsymbol{\eta}$  with Gaussian noise  $\boldsymbol{\eta} \sim \mathcal{N}(\mathbf{0}, \sigma^2 \mathbf{I})$ . The nonlinear coupling through the term  $(x_2 - x_1^2)^2$  makes direct sampling challenging. Following the constrained formulation presented above, we introduce an auxiliary variable  $z \in \mathbb{R}$  and write the constrained problem

$$\min_{\mathbf{x}, z} \frac{1}{2\sigma^2} \|\mathbf{y} - \mathbf{x}\|^2 + a(x_1 - \mu_0)^2 + (x_2 - z)^2 \quad \text{subject to} \quad z = x_1^2, \quad (29)$$

where  $\mathbf{x}$  plays the role of the model  $\mathbf{m}$ ,  $z$  plays the role of the wavefield  $\mathbf{u}$ , and  $z = x_1^2$  plays the role of the wave equation  $\mathbf{A}(\mathbf{m})\mathbf{u} = \mathbf{b}$ . The corresponding augmented Lagrangian (cf. equation 15) is

$$\mathcal{L}_\mu(\mathbf{x}, z, \varepsilon; \mathbf{y}) = \frac{1}{2\sigma^2} \|\mathbf{y} - \mathbf{x}\|^2 + a(x_1 - \mu_0)^2 + (x_2 - z)^2 - \varepsilon(z - x_1^2) + \frac{\mu}{2}(z - x_1^2)^2, \quad (30)$$

where  $\varepsilon$  is the Lagrange multiplier and  $\mu > 0$  the penalty parameter. Minimizing over  $z$  for fixed  $(\mathbf{x}, \varepsilon)$  gives the closed-form auxiliary update  $z = (2x_2 + \varepsilon + \mu x_1^2)/(2 + \mu)$ , after which the gradient  $\nabla_{\mathbf{x}} \mathcal{L}_\mu$  drives the SVGd particle update (equation 27) and the multiplier is updated via  $\varepsilon \leftarrow \varepsilon + \mu(x_1^2 - z)$ , progressively enforcing the constraint.

For the experiments, we set  $a = 0.5$ ,  $\mu_0 = 0$ ,  $\sigma = 0.5$ ,  $\mu = 1.0$ ,  $N_p = 1000$  particles, step size  $\eta = 0.15$ , and run for 2500 iterations. To isolate the effect of the constraint splitting, we also run standard SVGd (Algorithm 1) with the same number of particles, using the direct posterior gradient  $\nabla_{\mathbf{x}} \log p(\mathbf{x}|\mathbf{y})$ —without introducing auxiliary variables or multiplier updates. Because the coupled gradient is stiffer without the ADMM decomposition, standard SVGd requires a smaller step size ( $\eta = 0.05$ ) and more iterations (5000) to remain stable. Figure 1 shows the prior distribution alongside the noisy observations for four test instances.

Figure 2 displays the posterior distributions obtained by ADMM-SVGd for all four test instances. In each panel, the gray points show prior samples illustrating the banana-shaped Rosenbrock manifold, while the pink points represent posterior samples. The posteriors concentrate around the observations while respecting the prior structure, and in all instances the true underlying values (red triangles) lie within the posterior support. The constraint residual  $|z - x_1^2|$  remains below 0.1 across all instances (Figure 5), confirming that ADMM-SVGd enforces the nonlinear constraint  $x_2 \approx x_1^2$  even in the conditional setting.

Figure 3 overlays the posterior samples from both methods—ADMM-SVGd and standard SVGd—for the four test instances. The ADMM-SVGd samples (pink) tend to concentrate more tightly along the Rosenbrock manifold  $x_2 \approx x_1^2$ , whereas standard SVGd samples (green) exhibit somewhat broader spread. This is a consequence of the ADMM splitting: by explicitly enforcing  $z = x_1^2$  through the augmented Lagrangian, ADMM-SVGd keeps particles closer to the nonlinear manifold, while standard SVGd must rely on the coupled gradient alone to capture this structure. Furthermore, the stiff gradient coupling in the unsplit posterior forces standard SVGd to use a smaller step size ( $\eta = 0.05$  vs. 0.15) and twice the number of iterations (5000 vs. 2500). The quantile–quantile plots in Figure 4 compare the marginal distributions of the two methods, showing that both yield comparable marginals across the test instances. This manifold-adherent behavior of ADMM-SVGd is relevant to the FWI application, where the analogous

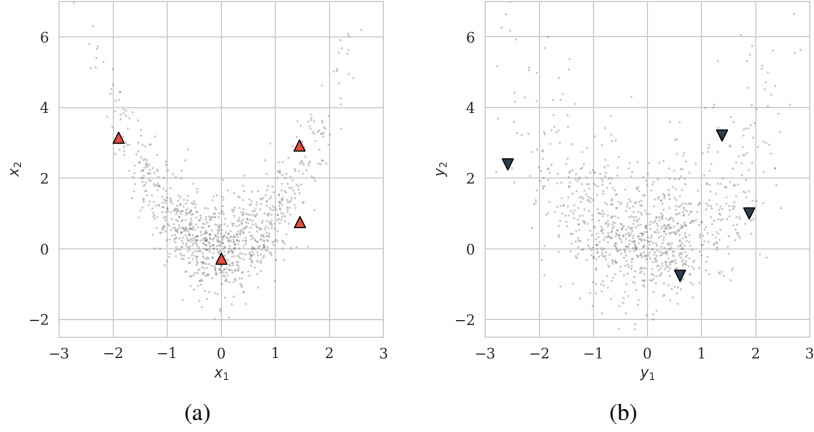


Figure 1: Overview of the conditional sampling problem. (a) Prior distribution  $p(\mathbf{x})$  (Rosenbrock) with four test instances (pink triangles). (b) Corresponding noisy observations with observation noise  $\sigma = 0.5$ .

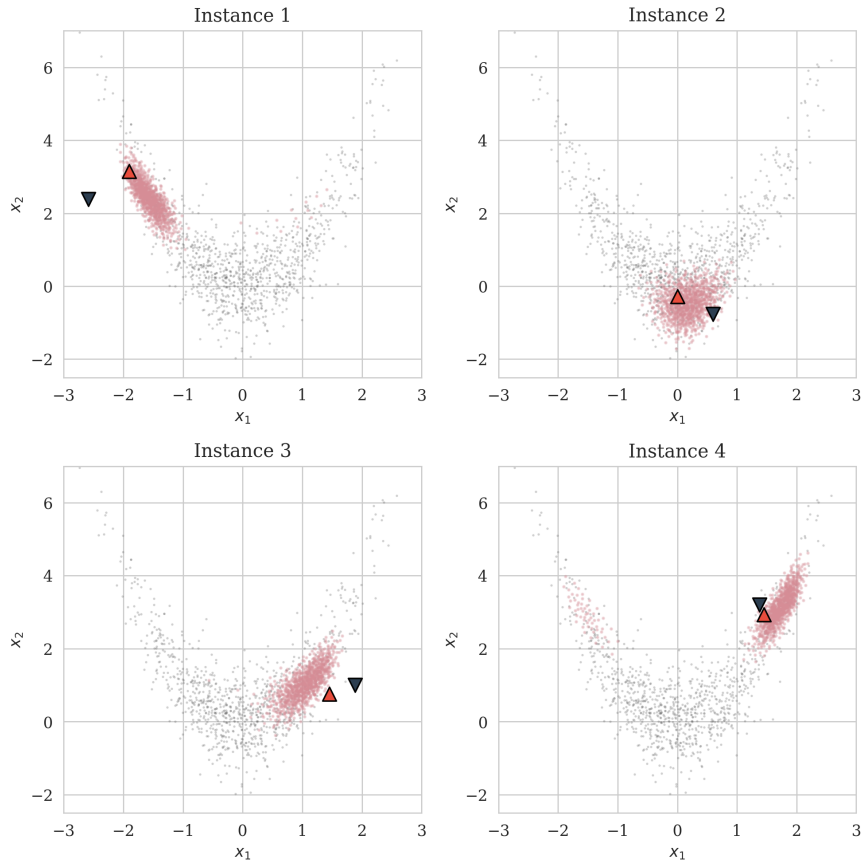


Figure 2: Posterior distributions for all four test observations obtained by ADMM-SVGD. Each panel shows prior samples (gray), ADMM-SVGD posterior samples (pink), the noisy observation ( $\nabla$ ), and the true value ( $\triangle$ ). The posteriors concentrate around the observations while remaining on the Rosenbrock manifold.

constraint—the wave equation—defines a manifold in the joint model-wavefield space that particles should respect to produce physically consistent samples.

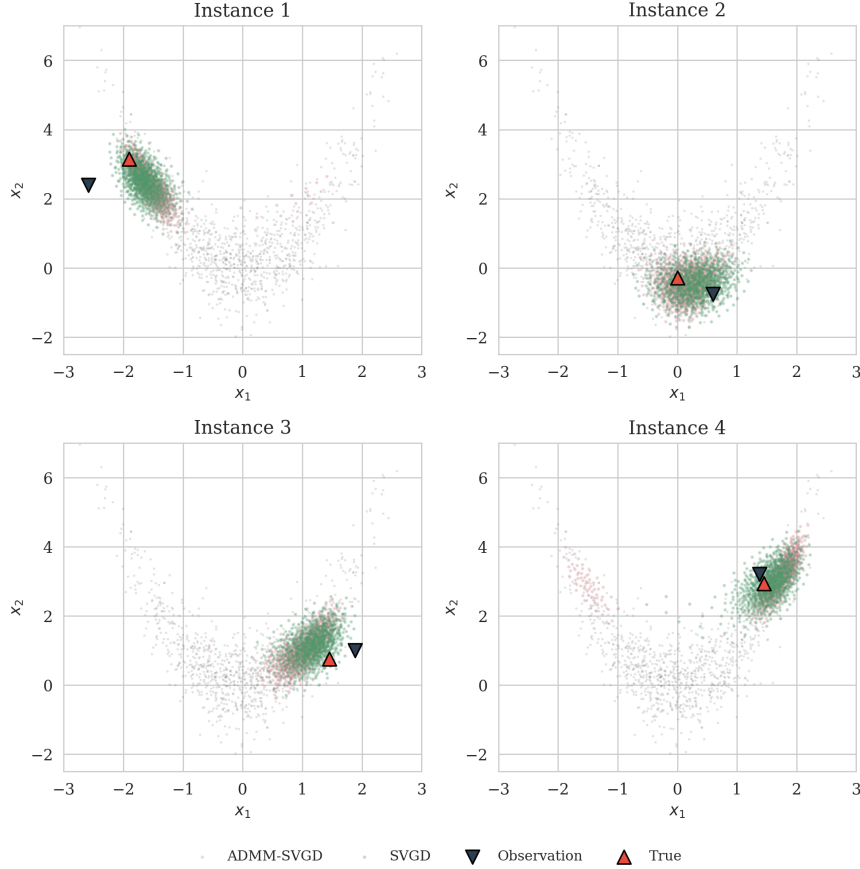


Figure 3: Combined posterior distributions for all four test observations from two methods: ADMM-SVGD (pink) and standard SVGD (green). The noisy observation ( $\nabla$ ) and true value ( $\triangle$ ) are shown in each panel.

Figure 5 shows the convergence diagnostics for ADMM-SVGD: the constraint residual  $|z - x_1^2|$  decreases over iterations, confirming that the ADMM mechanism progressively enforces the nonlinear constraint; the average log-posterior increases as particles move toward higher-probability regions; and the kernel bandwidth, posterior mean, and standard deviation all stabilize, indicating convergence of the particle ensemble.

## 7.2 Full waveform inversion

We now apply ADMM-SVGD to uncertainty quantification for full waveform inversion, where the wave equation constraint  $\mathbf{A}(\mathbf{m})\mathbf{u}_i = \mathbf{b}_i$  is enforced through the dual-space formulation (Algorithm 2). Although the model parameter  $\mathbf{m}$  represents the squared slowness, we display all results in terms of velocity for ease of interpretation. We present results on two velocity models of increasing complexity.

### 7.2.1 Prior distribution

We adopt a Gaussian random field (GRF) prior with a Matérn-type power spectrum [53] to encode smoothness and spatial correlation in the velocity model. The prior is defined in the spectral domain through the eigenvalues

$$\lambda(\mathbf{k}) \propto (4\pi^2|\mathbf{k}|^2 + \tau^2)^{-\alpha}, \quad (31)$$

where  $\mathbf{k}$  denotes the wavenumber vector,  $\tau$  controls the correlation length, and  $\alpha$  governs the smoothness of the realizations. Drawing samples from this prior reduces to generating independent standard normal coefficients in Fourier space, scaling them by  $\sqrt{\lambda(\mathbf{k})}$ , and applying the inverse fast Fourier transform.

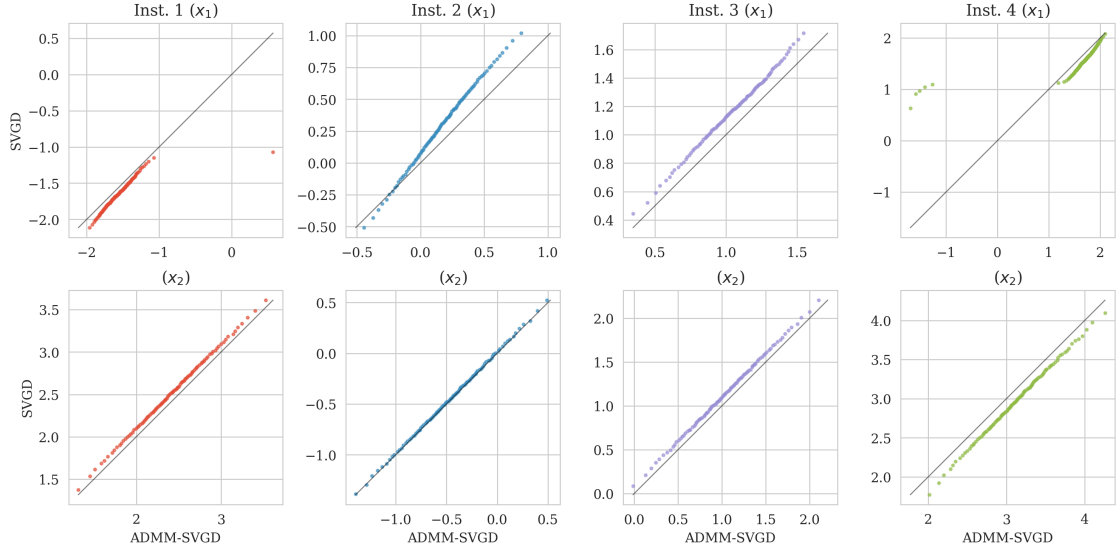


Figure 4: Quantile–quantile plots comparing the marginal distributions of standard SVGD against ADMM-SVGd for all four test instances. Each column corresponds to one instance; the top and bottom rows show the  $x_1$  and  $x_2$  marginals, respectively. Points on the diagonal indicate perfect agreement between the two methods.

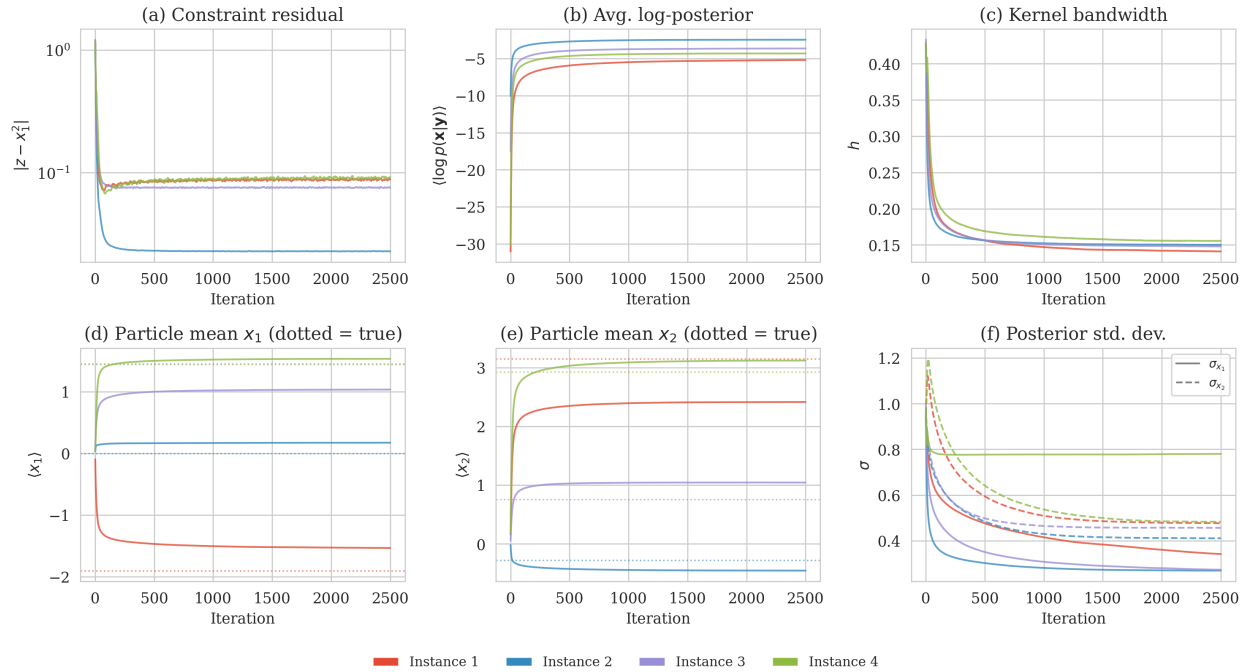


Figure 5: Convergence diagnostics for ADMM-SVGd across four test instances. (a) Constraint residual  $|z - x_1^2|$  decreasing to near zero. (b) Average log-posterior. (c) Kernel bandwidth. (d)–(e) Posterior mean for  $x_1$  and  $x_2$ . (f) Posterior standard deviation.

To ensure that the prior samples represent physically plausible squared-slowness values, we linearly rescale the zero-mean GRF realizations so that their values fall within a prescribed range  $[m_{\min}, m_{\max}]$ . Specifically, the mean is set to  $\bar{m} = (m_{\min} + m_{\max})/2$  and the standard deviation is scaled to  $\sigma_m = (m_{\max} - m_{\min})/6$ , so that approximately 99.7% of the sampled squared-slowness values lie within the target bounds. The choice of prior can significantly influence the posterior, particularly in under-determined inverse problems [54]. The score function  $\nabla_{\mathbf{m}} \log p_{\text{prior}}(\mathbf{m})$  required by SVGD is computed tractably in the spectral domain, where the covariance is diagonal, reducing the matrix inversion to elementwise division of the Fourier coefficients by the eigenvalues. Representative samples from this prior are shown in Figure 6b.

### 7.2.2 Gaussian anomaly model

We first consider a controlled setting in which the true subsurface model consists of a Gaussian low-velocity anomaly embedded in a homogeneous background of 2 km/s. The model spans 2 km in both horizontal distance and depth, discretized on a regular grid. The survey employs 50 sources emitting Ricker wavelets with a dominant frequency of 6 Hz at the top of the model, while 200 receivers are distributed along the bottom (Figure 6). The particles are initialized from random velocity fields drawn from the prior distribution, which bear no resemblance to the true model. The inversion proceeds via multiscale frequency continuation [55] from 4 Hz to 6 Hz. For each data frequency, the inversion is performed over a maximum of 30 iterations.

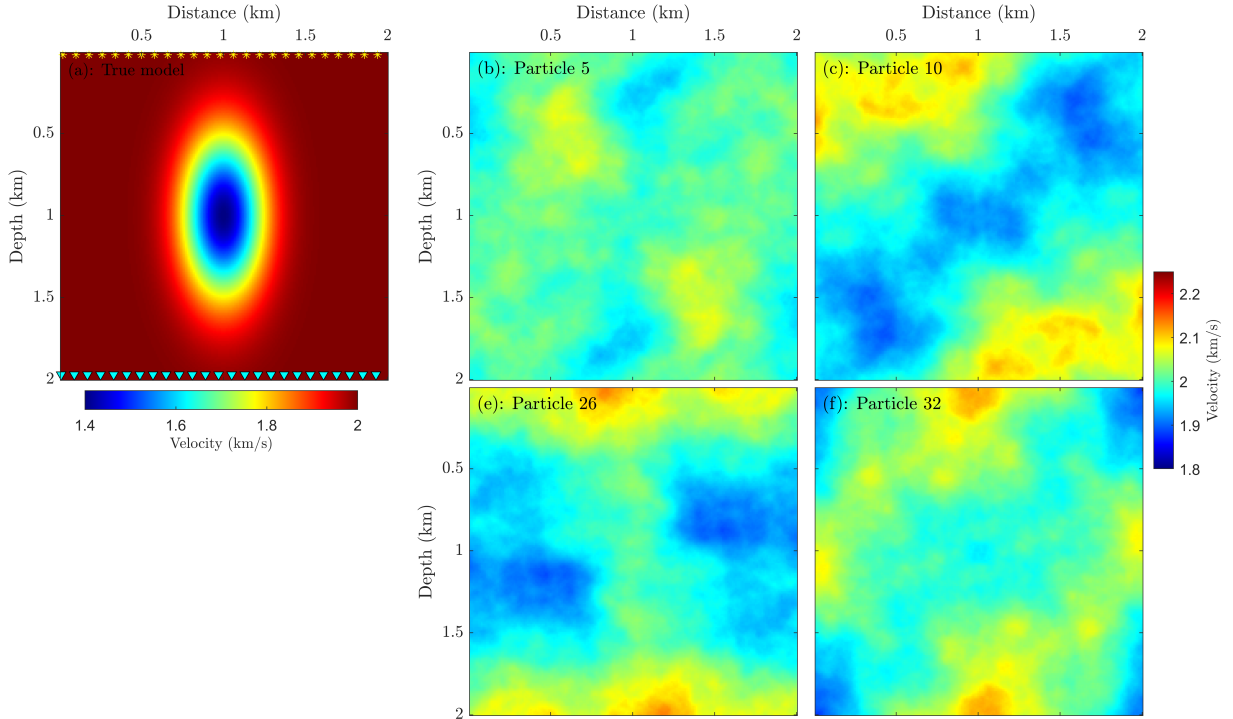


Figure 6: Gaussian anomaly model setup. Left: true velocity model consisting of a low-velocity anomaly in a homogeneous background, with sources (colored dots) along the surface and receivers along the bottom. Right: four representative prior velocity particles showing the initial ensemble.

Figure 7 shows the evolution of the conditional mean estimate (top row) and the pointwise standard deviation (bottom row) across frequencies. As the inversion progresses from 4 Hz to 6 Hz, the conditional mean progressively recovers the true velocity structure, with the relative model error ( $\text{RME} = \frac{\|m^* - m\|_2}{\|m^*\|_2}$ ) decreasing from 6.43% to 6.03%. The pointwise standard deviation provides a spatially resolved assessment of uncertainty: it is largest at the boundaries of the anomaly—where the velocity contrast creates the strongest sensitivity to perturbations—and near the bottom of the model where illumination from the surface sources is weakest. In the background regions where the data provide strong constraints, the standard deviation is small. This spatially varying uncertainty pattern is physically consistent with the acquisition geometry and the subsurface structure.

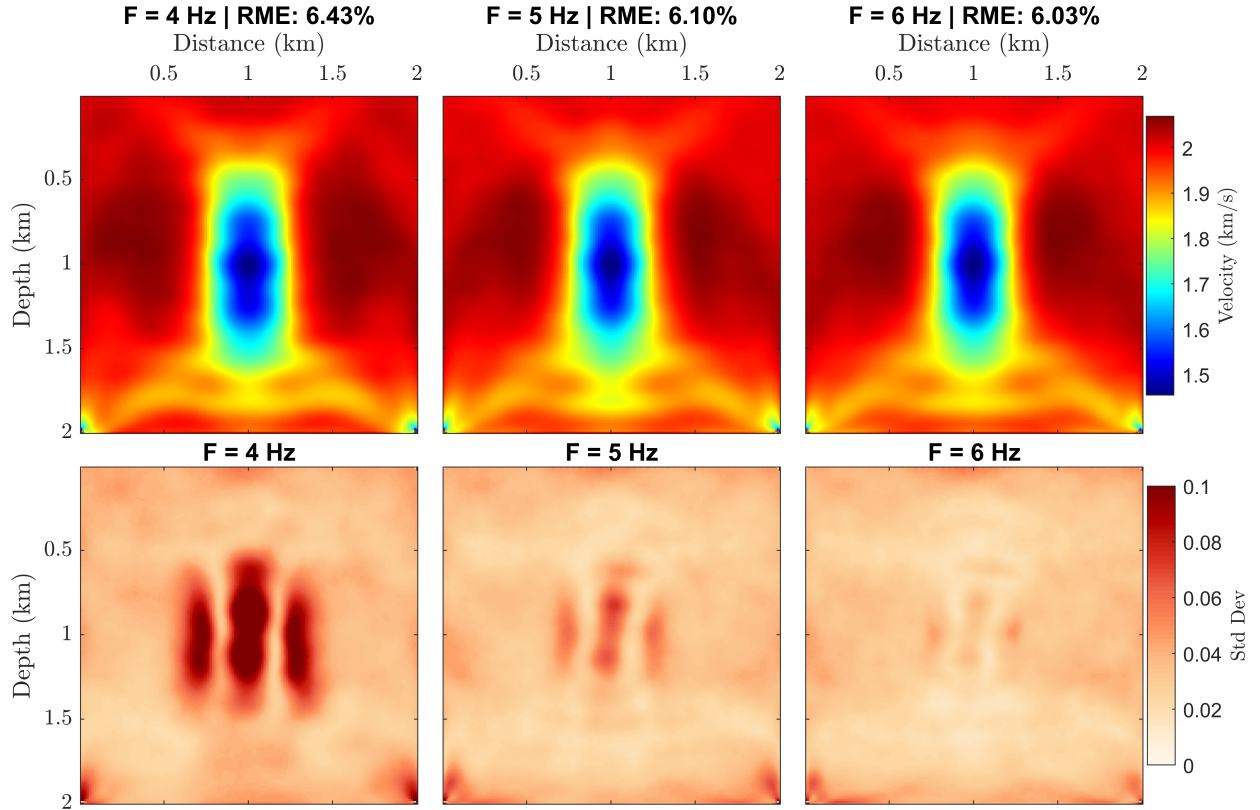


Figure 7: Evolution of posterior statistics across frequencies for the Gaussian anomaly model. Top row: conditional mean velocity estimate at 4, 5, and 6 Hz with corresponding model errors. Bottom row: pointwise standard deviation showing uncertainty concentrated at the anomaly boundaries and at depth.

To further assess the quality of the uncertainty estimates, we extract vertical velocity profiles at three horizontal locations ( $x = 0.8, 1.0,$  and  $1.2$  km) through the center of the anomaly (Figure 8). The posterior mean (solid blue) closely tracks the true model (dashed black), and the 68%, 95%, and 99% credible intervals (blue shading) contain the true velocity profile throughout the depth range. The credible intervals are widest between 0.6 and 1.4 km depth, where the velocity deviates most from the background and the inverse problem is most sensitive to model perturbations. At the center of the anomaly ( $x = 1.0$  km), the true value remains well within the 95% credible interval. The widening of the credible intervals in the anomaly region reflects the increased sensitivity to model perturbations where the velocity deviates most from the background, while the modest additional broadening near the base of the model is consistent with the decreasing resolution of the surface acquisition geometry. This spatially varying uncertainty pattern confirms that ADMM-SVGD produces well-calibrated uncertainty estimates.

### 7.2.3 Marmousi II model

We next apply ADMM-SVGD to the Marmousi II velocity model [56], a widely used benchmark featuring complex geological structures including dipping layers, faults, anticlinal traps, and strong lateral velocity variations. The model is 17.1 km wide and 3.5 km deep, discretized with a 25 m grid interval (Figure 9a). We use the same GRF prior as in the Gaussian anomaly example, but add a linearly increasing background velocity with depth to the prior samples for initialization, reflecting the general trend of velocity increasing with burial depth (Figure 9b).

The inversion is carried out in two multiscale frequency-domain cycles, each spanning the range 3–12 Hz with a 0.5 Hz frequency increment. For frequencies below 7 Hz, we perform 20 iterations per frequency, while frequencies above 7 Hz use 10 iterations. The final particle ensemble obtained at the end of the first cycle is used as the initial ensemble for the second cycle. To investigate the effect of data coverage on the posterior distribution, we run three acquisition configurations with  $N_s = 17, 34,$  and 68 sources uniformly distributed along the surface. In all acquisition configurations, a Ricker wavelet with a dominant frequency of 8 Hz is used as the source signature, and we employ

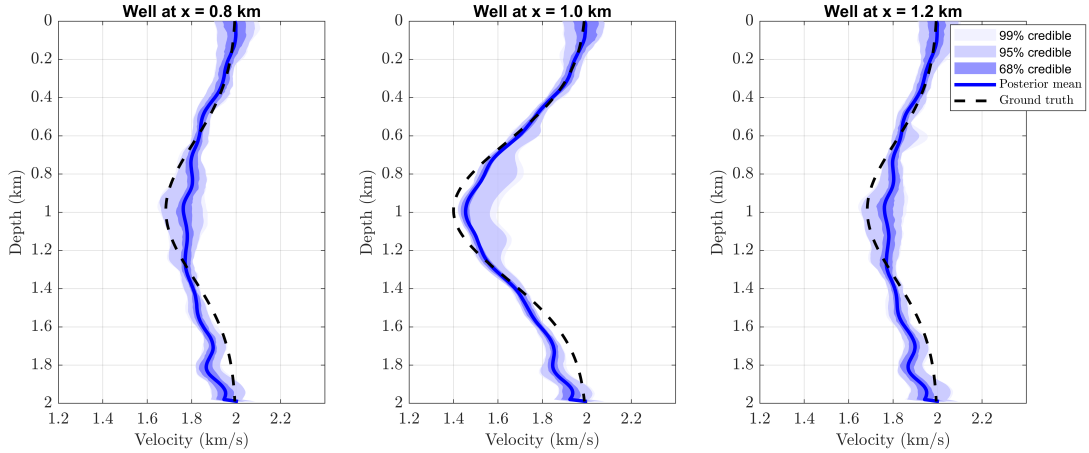


Figure 8: Vertical velocity profiles at three horizontal locations through the Gaussian anomaly. The posterior mean (solid blue) closely tracks the true model (dashed black). The shaded regions correspond to 68%, 95%, and 99% credible intervals, which contain the true velocity and are widest in the anomaly region.

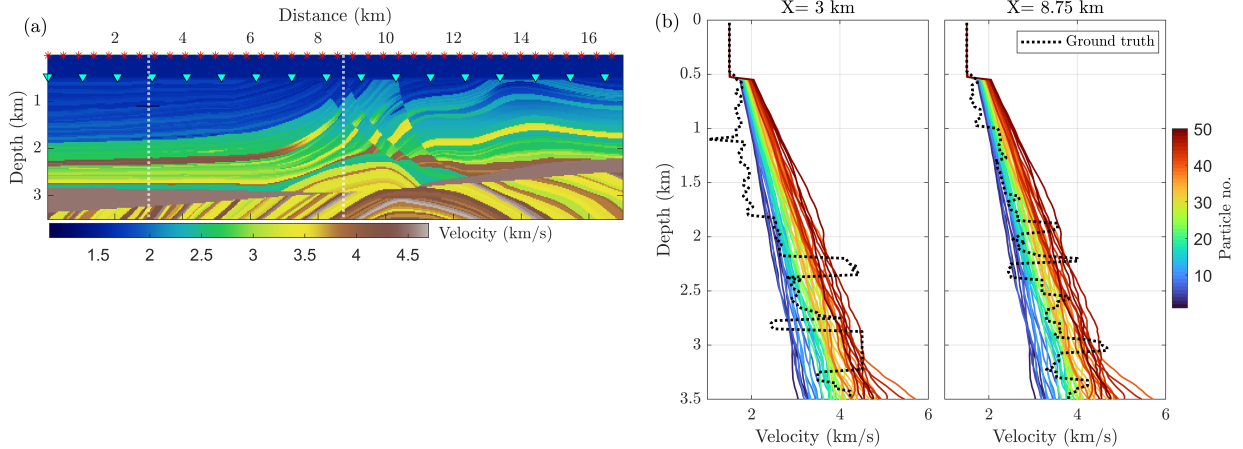


Figure 9: Marmousi II P-wave velocity model (a) with inverted triangles denoting receiver locations and red stars indicating source positions. (b) Comparison of velocity profiles at  $X = 3$  km and  $X = 8.75$  km corresponding to the white dashed line in (a). Colored lines represent the ensemble of initial particles, while the black dotted line indicates the ground-truth model.

114 receivers that are uniformly spaced at intervals of 150 m along the surface. The inversion follows a multiscale frequency continuation strategy [55].

Figure 10 shows the evolution of the conditional mean velocity estimate across inversion cycles and frequencies, organized by cycle-frequency (rows) and source number (columns). In the first cycle at low frequencies (3–5 Hz), the conditional mean recovers only the large-scale background structure of the model. As higher frequencies are introduced and the inversion advances into the second cycle, structural details such as dipping reflectors, anticlines, and lateral velocity contrasts become progressively sharper. The relative model error decreases systematically across cycles for all source configurations.

The corresponding pointwise posterior standard deviation is presented in Figure 11. Early in cycle 1, the uncertainty is broadly distributed across the model. As the inversion progresses through the frequency schedule and into cycle 2, the standard deviation decreases throughout the model—most notably in the shallow section, where the surface acquisition provides strong illumination. The uncertainty remains persistently elevated at depth and near the model boundaries, reflecting the inherent limitations of surface-based seismic acquisition for resolving deep structure.

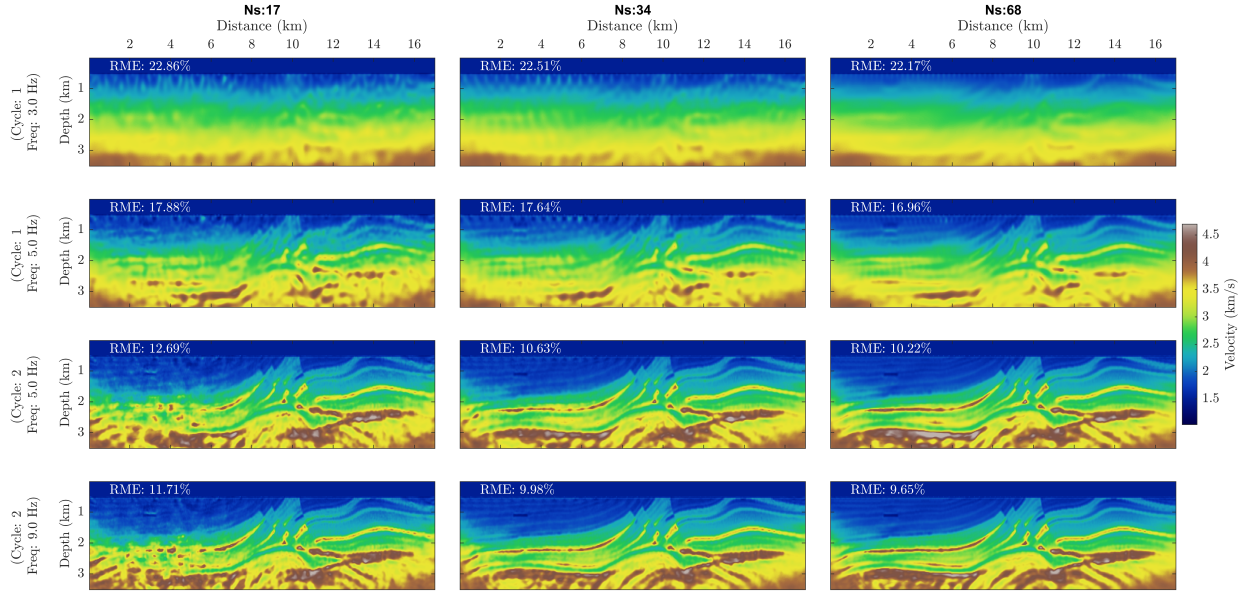


Figure 10: Conditional mean velocity models obtained at successive inversion stages (cycles 1-2) and frequencies, shown for  $N_s = 17, 34, 68$  (left to right). Each row corresponds to a given cycle–frequency pair, while each column shows the conditional mean estimate for a specific  $N_s$ . Reported RME values quantify the reduction of model error across cycles.

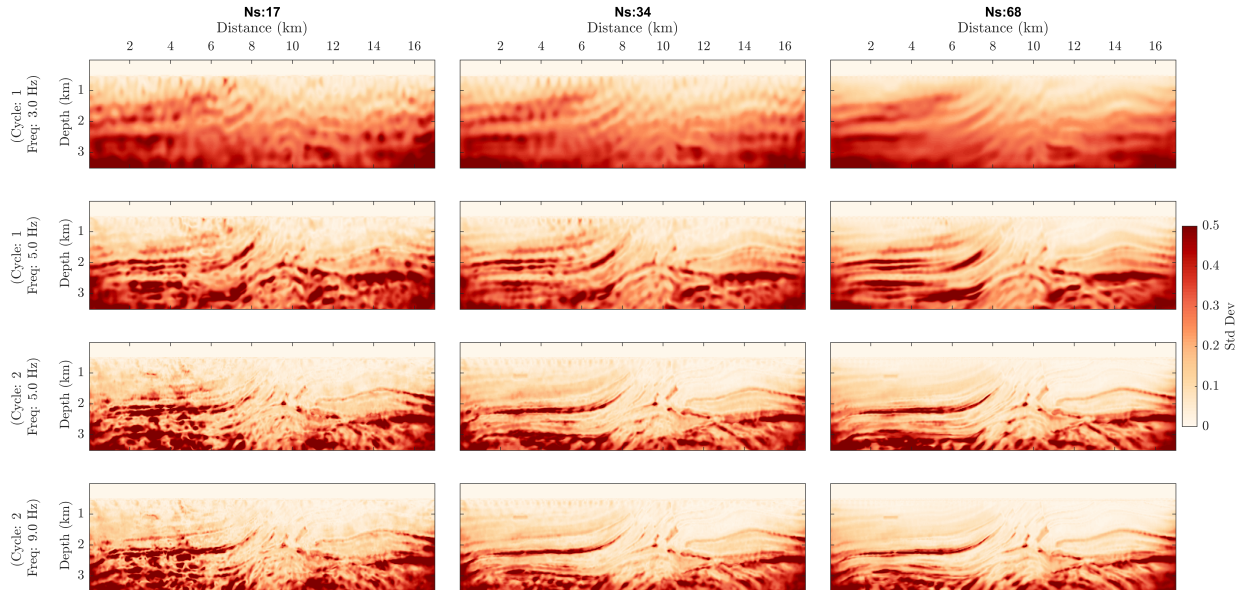


Figure 11: Pointwise posterior standard deviation of the velocity field for the same inversion stages and ensemble sizes shown in Figure 10.

Figures 12–14 show the velocity estimates of three representative particles (indices 10, 20, and 40) across inversion stages for  $N_s = 17$ , 34, and 68 sources, respectively. These particle-level views complement the ensemble statistics shown in Figures 10 and 11 by illustrating the diversity of models that collectively represent the posterior. At the start of cycle 1, the individual particles differ markedly from one another and from the true model, reflecting the variability of the prior. As the inversion progresses, the particles converge toward consistent large-scale features—particularly in the shallow section—while retaining particle-specific differences in fine-scale structure and at depth. This residual spread reflects genuine posterior uncertainty rather than inversion instability. Comparing across source configurations, interparticle variability decreases markedly as the number of sources increases, consistent with stronger posterior contraction under improved data coverage.

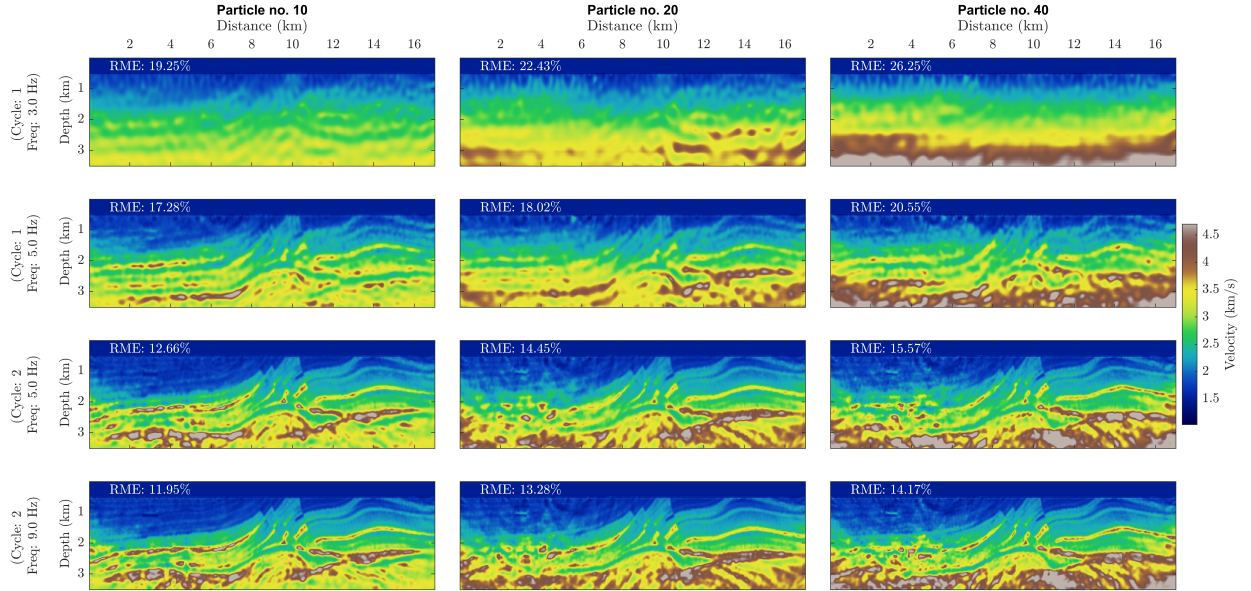
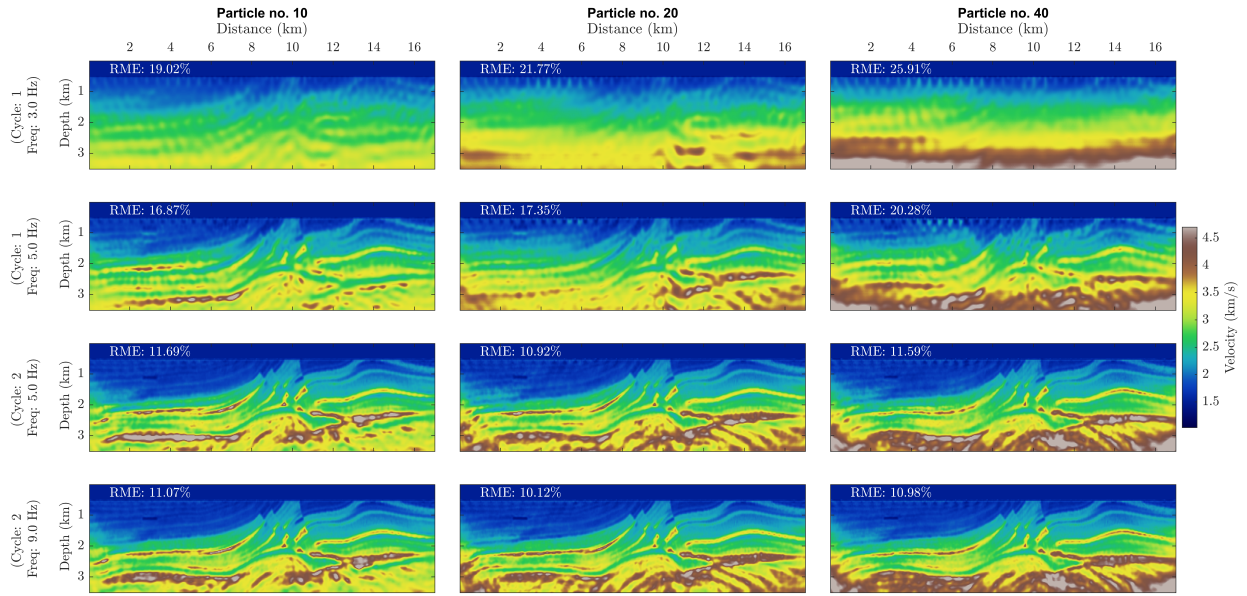
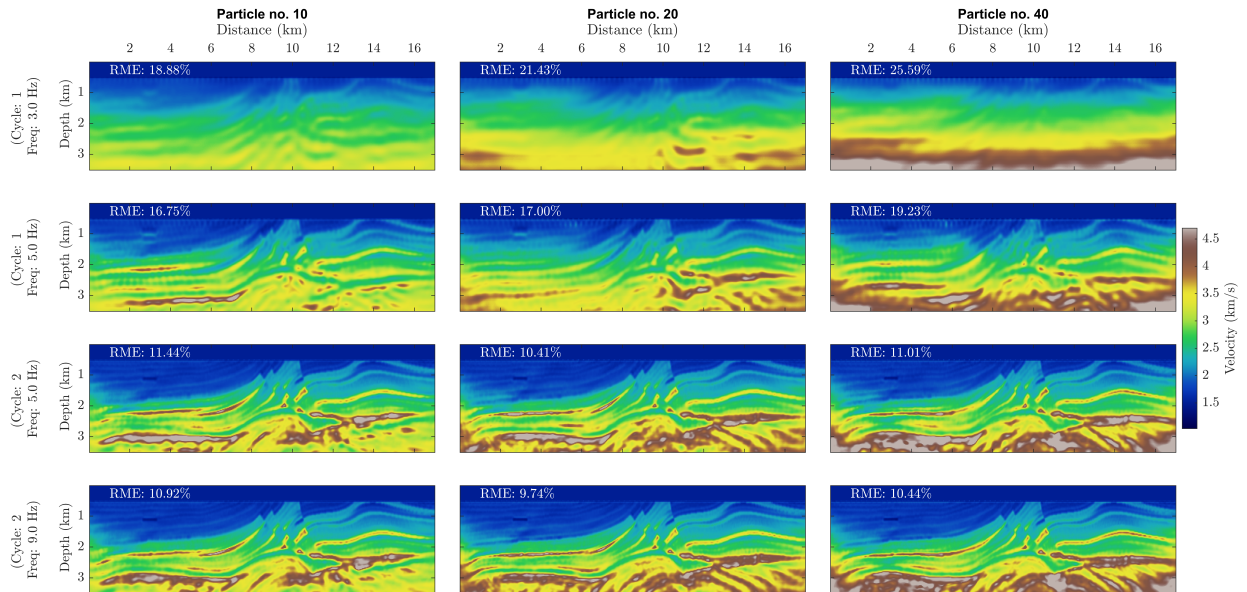


Figure 12: Conditional mean velocity estimates for three particles (particle indices 10, 20, and 40) obtained using  $N_s = 17$  seismic sources. Each column corresponds to one particle, while each row shows the inversion state at successive cycle–frequency stages.

Figure 15 summarizes the final inversion results for the three source configurations. The top row displays the conditional mean velocity estimates, which improve as the number of sources increases—the relative model error (RME) decreases from 11.47% ( $N_s = 17$ ) to 9.81% ( $N_s = 34$ ) and 9.50% ( $N_s = 68$ ). The conditional mean captures the major geological features of the Marmousi model, including the dipping reflectors, the anticlinal structures, and the velocity inversions at depth. The middle row shows the pointwise standard deviation, which serves as a spatially resolved uncertainty map. With  $N_s = 17$  sources, the uncertainty is broadly distributed, reflecting the limited data coverage. As the number of sources increases to 34 and 68, the pointwise standard deviation decreases—particularly in the shallow section where the denser source coverage provides better illumination. The uncertainty remains elevated in the deep section of the model and near the lateral boundaries, consistent with the reduced sensitivity of surface measurements to deep structures. The bottom row depicts the difference between the conditional mean and the true velocity model. Notably, the error and standard deviation maps are strongly correlated—regions of large estimation error coincide with regions of high posterior uncertainty, and both increase systematically with depth. This spatial agreement quantitatively confirms that the uncertainty estimates produced by ADMM-SVGD are well-calibrated, despite operating in a high-dimensional parameter space.

The convergence behavior underlying these results is summarized in Figure 16. The mean pointwise standard deviation (Figure 16a) decreases over iterations for all source configurations, indicating progressive posterior contraction as the data constraints are assimilated. The relative model error (Figure 16b) shows a consistent decreasing trend, with the rate of decrease being faster for larger numbers of sources. For  $N_s = 68$ , the RME drops below 10% within approximately 300 iterations, whereas with  $N_s = 17$  the error plateaus around 11.5%. This behavior is consistent with the expected Bayesian posterior contraction property: more observed data leads to a more concentrated posterior and a more accurate conditional mean estimate.

Figure 13: Same as Figure 12 but for  $N_s = 34$ .Figure 14: Same as Figure 12 but for  $N_s = 68$ .

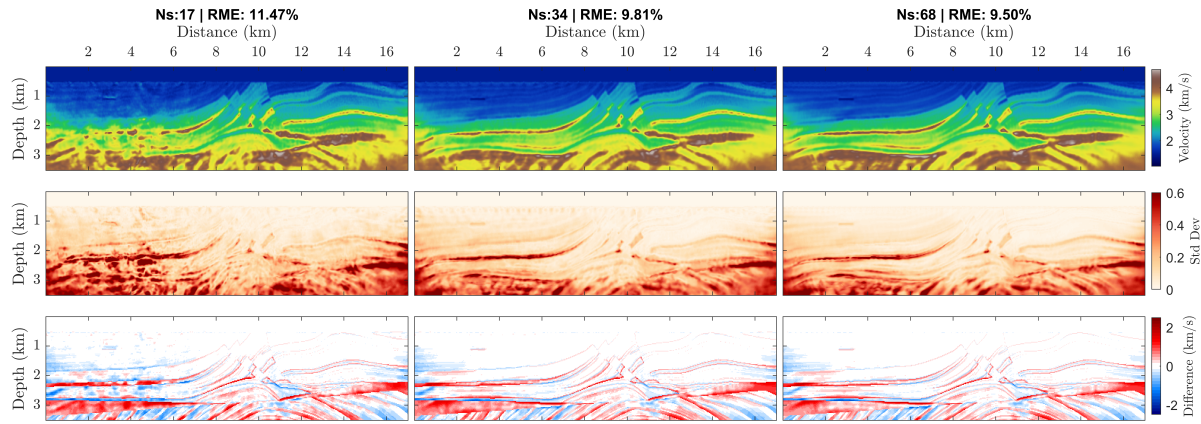


Figure 15: Marmousi II inversion results for  $N_s = 17, 34,$  and  $68$  sources (left to right). Top row: conditional mean velocity estimates with relative model errors. Middle row: pointwise standard deviation. Bottom row: difference between conditional mean and true velocity model.

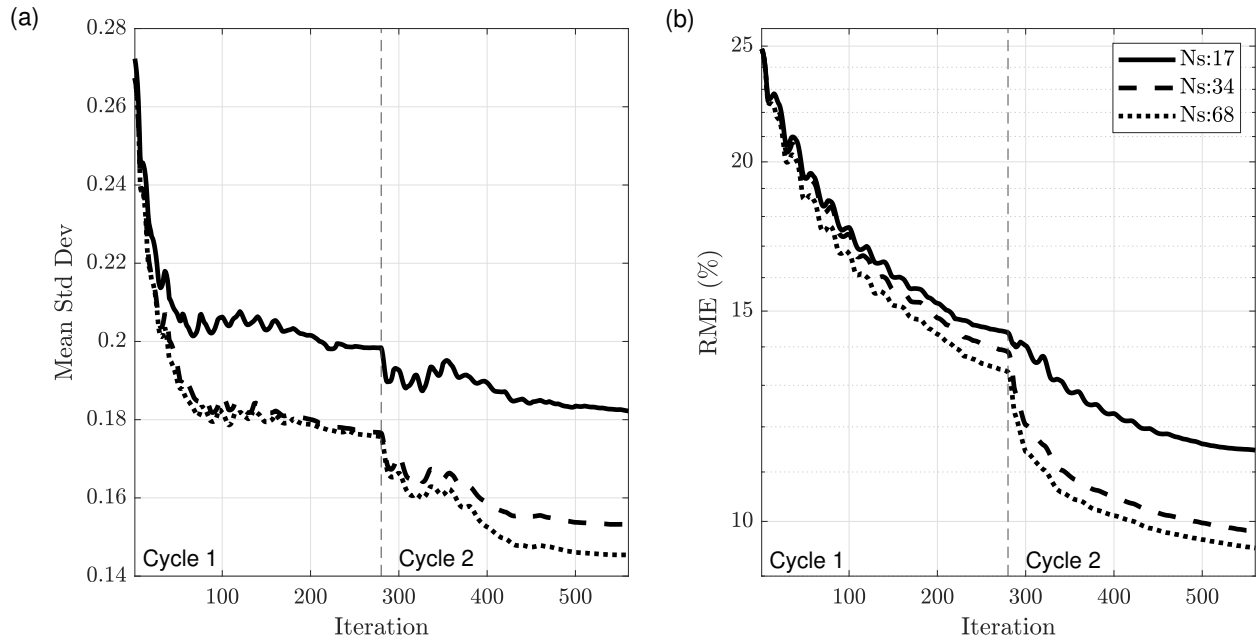


Figure 16: Convergence behavior for the Marmousi II model. (a) Mean pointwise standard deviation versus iteration. (b) Relative model error versus iteration. Both quantities decrease with iteration count and with increasing source coverage, confirming posterior contraction. The vertical dashed line separates inversion cycles.

To examine the depth-dependent structure of the posterior, Figure 17 shows vertical profiles of the normalized posterior probability density at three lateral positions across the model ( $X = 2.75, 5.0, 8.75$  km). At each depth, the color intensity represents the probability density over velocity, with the true velocity overlaid as a red dotted curve. In the shallow section, the posteriors are tightly concentrated around the true velocity for all source configurations, reflecting the strong data constraints near the surface. With increasing depth, the posterior densities broaden and, in geologically complex regions, develop multimodal structure—indicating that several velocity values are consistent with the observed data. As the number of sources increases from  $N_s = 17$  to 68, the posteriors sharpen and the probability mass concentrates more tightly around the true velocity. This posterior contraction with increasing data coverage is a hallmark of well-calibrated Bayesian inference: each additional source provides independent constraints on the subsurface velocity, reducing the volume of model space consistent with the data and yielding tighter credible intervals. The persistent broadening at depth, irrespective of source count, reflects the intrinsic resolution limits of surface-based seismic acquisition geometry.

Zooming into specific locations, Figure 18 displays pointwise posterior probability density estimates at four positions in the model, each corresponding to a different geological setting. At the shallow location ( $z = 0.82$  km,  $x = 2.75$  km), the posteriors are unimodal and tightly concentrated around the true velocity (dashed black), with increasing sharpness as the number of sources grows. The prior (red) is broad and uninformative, while the posteriors contract progressively toward the ground truth. At deeper and more geologically complex locations, the posterior distributions become broader and, in some cases, multimodal—reflecting genuine ambiguity in the velocity structure that cannot be resolved by the available data. For instance, at ( $z = 2.4$  km,  $x = 5.0$  km), the posteriors exhibit multiple peaks corresponding to plausible velocity values at this depth, with the multimodality diminishing as more sources are added. This capacity to reveal multimodal uncertainty at geologically complex locations is particularly valuable for risk assessment in geophysical applications, where identifying the full range of plausible models is as important as obtaining a single point estimate.

**Noise case.** To investigate the effect of noise, we repeat the Marmousi II experiment with complex-valued Gaussian noise added to the frequency-domain data independently at each frequency. For a given noise level, the noise standard deviation is defined as a fixed percentage of the maximum absolute value of the data,  $\sigma = \alpha \max(|d|)$ , where  $\alpha = 0.10, 0.15$  and  $0.20$  correspond to 10%, 15%, and 20% noise levels, respectively. The noise realization is generated as

$$e = \frac{\sigma}{\sqrt{2}} (\mathcal{N}(0, 1) + i\mathcal{N}(0, 1)),$$

which ensures equal variance in the real and imaginary components. All other experimental settings—acquisition geometry, prior specification, frequency schedule, and number of particles—are kept identical to the noise-free case with  $N_s = 34$  sources, allowing the effect of noise to be isolated. Figure 19 compares the magnitude of the 3 Hz data in the source–receiver coordinate system for the noise-free case and for increasing noise levels. In the absence of noise, the magnitude plot shows a clear and coherent diagonal energy pattern, reflecting the dominant source–receiver response at this low frequency. As the noise level increases from 10% to 20%, the background becomes progressively more contaminated by random fluctuations, leading to a gradual reduction in contrast and continuity of the coherent energy trend. In a Bayesian framework, the noise level directly informs the likelihood function and hence the balance between data fidelity and prior regularization, effectively serving as a principled mechanism for regularization parameter selection. Figure 20 presents the inversion results under the three noise levels, organized in the same format as Figure 15: the top row shows the conditional mean velocity estimate with its corresponding RME, the middle row shows the pointwise posterior standard deviation, and the bottom row shows the difference between the conditional mean and the true model. The conditional mean estimates remain geologically coherent across all noise levels, successfully recovering the major structural features of the Marmousi II model, including the dipping reflectors and anticlinal structures. However, the RME increases monotonically with noise level from 10.28% at 10% noise to 11.04% at 15% and 12.20% at 20%, reflecting the reduced information content of the contaminated data and the increased difficulty of distinguishing signal from noise. Figure 21 shows vertical profiles of the normalized posterior probability density at the same three lateral positions as Figure 17 ( $X = 2.75, 5.0$ , and  $8.75$  km), now for data contaminated with noise. The structure of these profiles mirrors the depth-dependent behavior observed in the noise-free case, but with systematically broader posterior bands at all depths and noise levels. In the shallow section, the posteriors remain approximately unimodal and concentrated near the true velocity across all noise levels, though the concentration is visibly looser than in the noise-free case. With increasing depth, the posterior densities broaden further and the multimodal structure observed in the noise-free case (cf. Figure 17) becomes more pronounced, particularly at 20% noise where the probability mass spreads over a wider range of velocities. This progressive degradation with noise level is consistent with the reduced signal-to-noise ratio and confirms that the method responds appropriately to the diminished information content of the data.

Figure 22 summarizes the convergence behavior of the inversion under the three noise levels. The mean pointwise standard deviation (Figure 22a) decreases over iterations for all noise levels, confirming that the ADMM multiplier

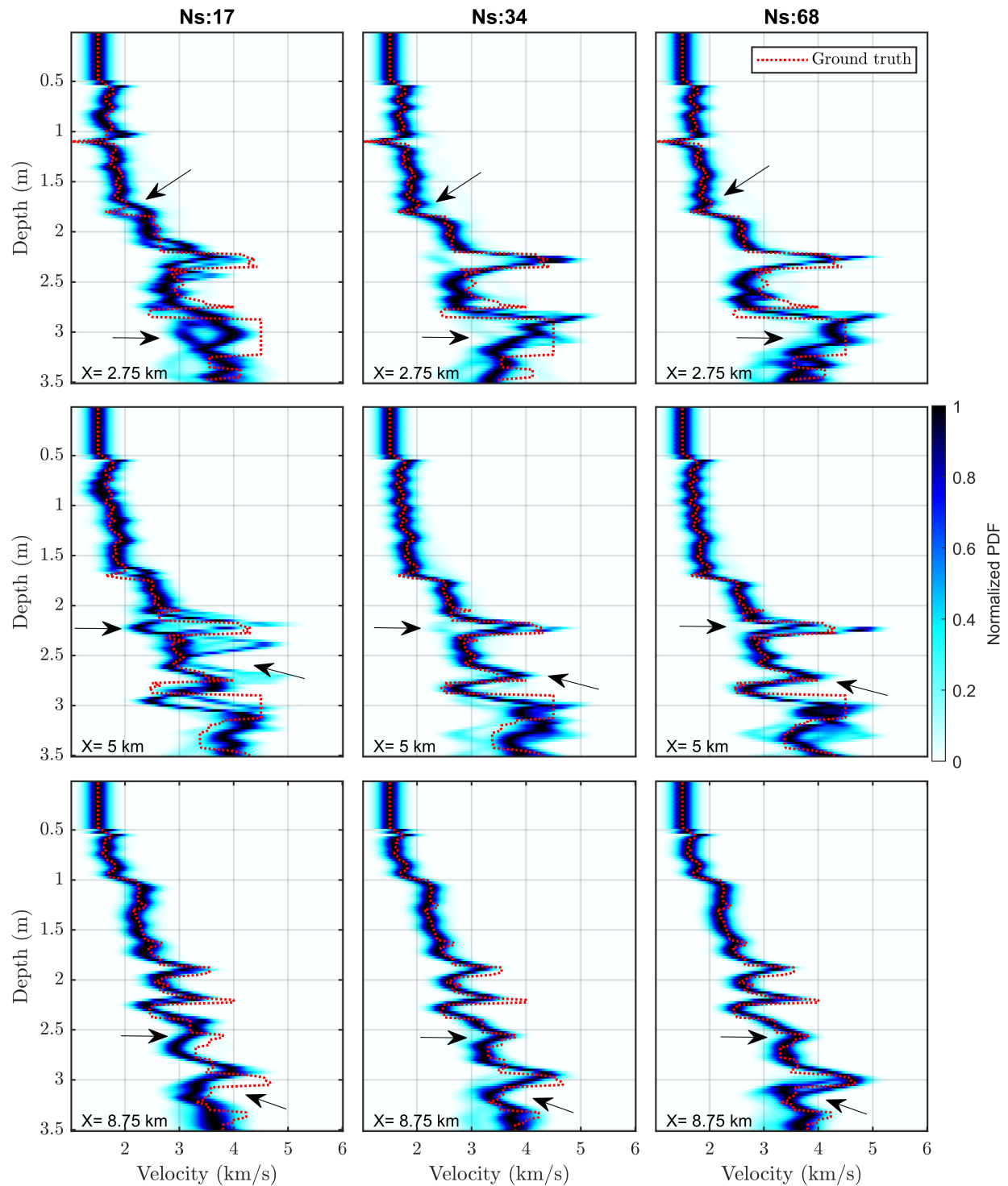


Figure 17: Vertical profiles of the normalized posterior probability density at three lateral positions in the Marmousi II model for  $N_s = 17, 34,$  and  $68$  sources (left to right). The true velocity profile is overlaid in dotted red. The posteriors sharpen and concentrate around the true velocity as the number of sources increases, while multimodal structure at depth reflects genuine geological ambiguity.

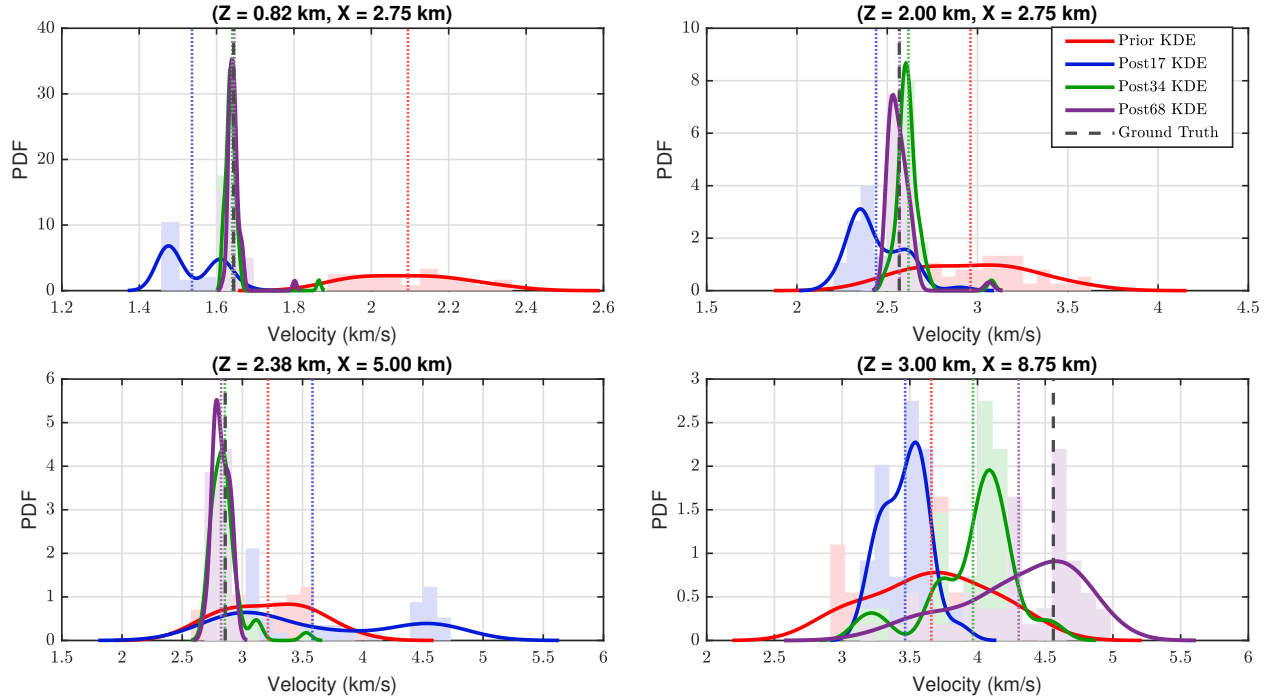


Figure 18: Pointwise posterior probability density estimates at four locations in the Marmousi II model for  $N_s = 17$ , 34, and 68 sources. The prior (red) is broad, while the posteriors contract toward the ground truth (dashed black) with increasing source coverage. At complex geological locations, the posteriors exhibit multimodality reflecting genuine velocity ambiguity.

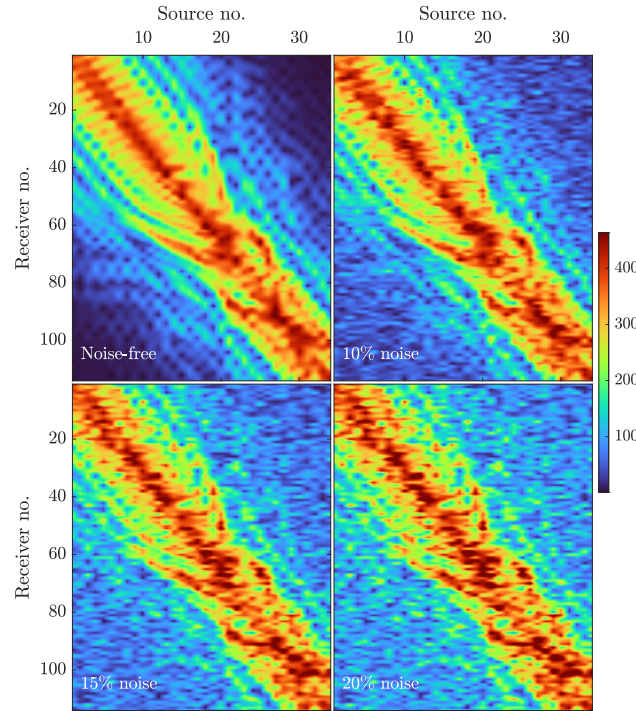


Figure 19: Magnitude plots of the 3 Hz data in the source–receiver domain under different noise levels. The top-left panel shows the noise-free data, while the remaining panels correspond to 10%, 15%, and 20% complex Gaussian noise added independently at each frequency.

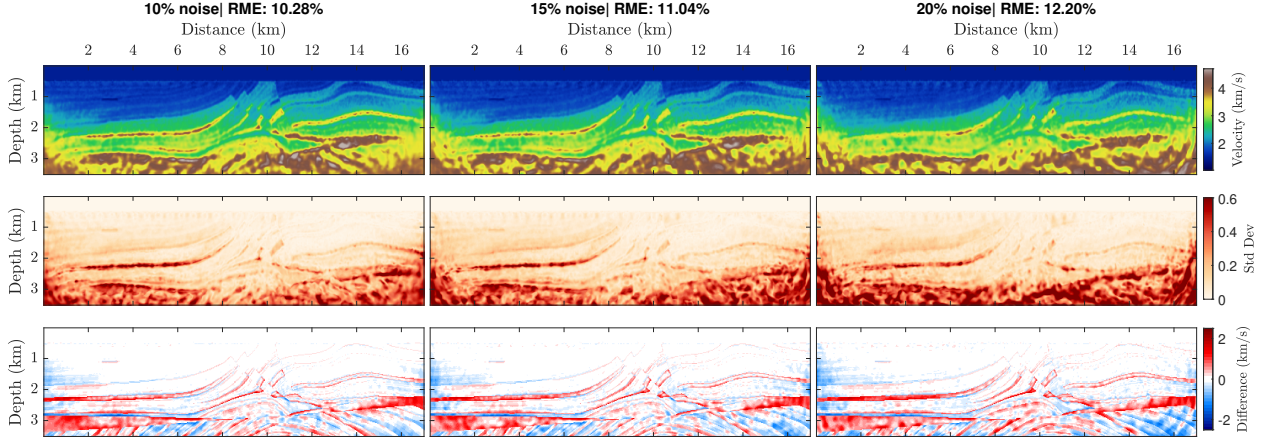


Figure 20: Inversion results for the Marmousi II model under increasing noise levels (left to right). Top row: conditional mean velocity estimates with corresponding relative model errors (RME). Middle row: pointwise posterior standard deviation, representing model uncertainty. Bottom row: difference between the conditional mean estimate and the true velocity model.

updates and frequency continuation schedule successfully drive posterior contraction regardless of the noise regime. However, the rate of contraction is slower and the asymptotic level is higher for noisier data: at 20% noise, the standard deviation plateaus at a value substantially above the noise-free case, reflecting higher uncertainty. The inset boxes in Figure 22 provide a quantitative summary of the asymptotic behavior by reporting the final RME and mean pointwise standard deviation at convergence for each noise level. Examining these terminal values reveals a consistent trend: both quantities increase approximately linearly with the noise level. Since the posterior precision scales inversely with the noise variance  $\sigma^2$  under a Gaussian likelihood, higher noise levels lead to broader posteriors and, consequently, larger pointwise standard deviations. The approximately linear relationship between noise level and terminal RME further suggests that the conditional mean degrades gracefully under increasing noise contamination—rather than exhibiting abrupt failure modes—corroborating the robustness of the conditional mean estimator discussed in Section 3.1.

Figure 23 provides a detailed view of per-particle 2-norm data residual evolution across iterations and frequencies for the three noise levels, offering insight into the fitting behavior of the individual particles and the ensemble as a whole. Each colored line tracks an individual particle’s residual—with color encoding the particle index—while the black solid line denotes the ensemble mean. The residual curves exhibit a characteristic sawtooth-like pattern arising from the multiscale frequency continuation strategy: at each frequency transition the residual increases abruptly as higher-frequency data are introduced, then decreases monotonically within each stage as the particles adapt their velocity models accordingly. Across all noise levels and both cycles, the ensemble mean residual approaches but does not systematically undercut the noise level lines, confirming that ADMM-SVGD achieves a data fit that avoids overfitting. The broader particle distributions at higher noise levels are consistent with the wider posteriors reported in Figures 20–22. The markedly lower residual starting point at the beginning of cycle 2 across all panels further demonstrates the benefit of warm-starting from the cycle 1 ensemble, accelerating convergence within each subsequent frequency stage.

## 8 Discussion

The numerical results presented above demonstrate that ADMM-SVGD can produce well-calibrated posterior samples for constrained inverse problems across a range of problem sizes and complexities. Several aspects of the method merit further discussion.

The per-iteration cost of ADMM-SVGD is dominated by the auxiliary variable solves, each of which requires one application of  $\mathbf{A}(m)^{-1}$ . For  $N_p$  particles and  $N_s$  sources, the total cost per outer iteration is  $O(N_p \times N_s)$  forward solves. This cost is mitigated by the embarrassingly parallel structure: all particle-source combinations can be computed independently. Furthermore, the dual-space formulation avoids explicit adjoint solves, as the gradient information is embedded in the auxiliary variable updates, reducing the implementation complexity compared to adjoint-based sampling methods.

The penalty parameter  $\mu$  plays a dual role: it controls the rate at which the wave equation constraint is enforced and, through the probabilistic interpretation, determines the width of the augmented posterior relative to the true posterior.

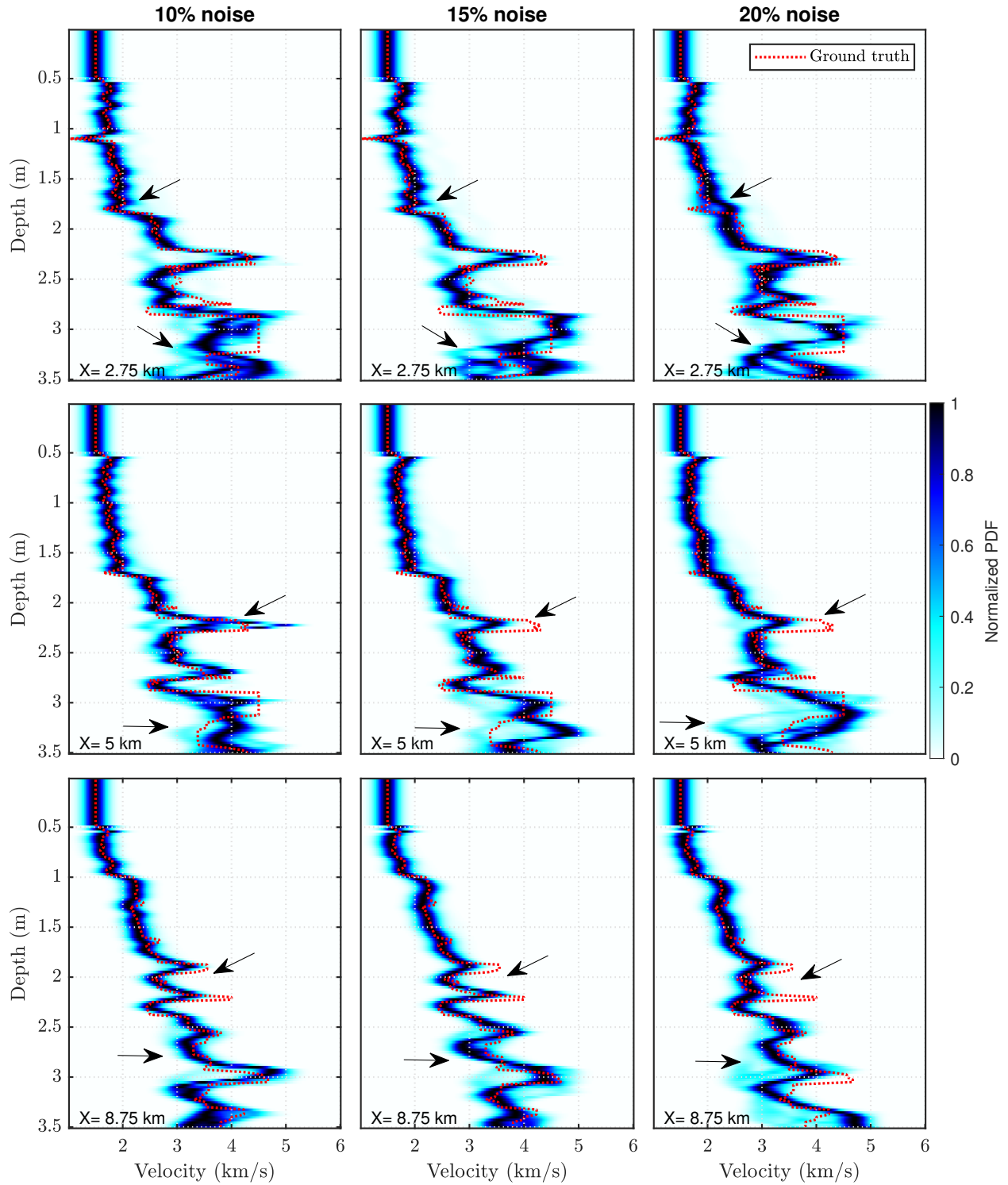


Figure 21: Vertical profiles of the normalized posterior probability density at three lateral positions in the Marmousi II model for  $N_s = 34$ , shown for data contaminated with 10%, 15%, and 20% noise (left to right). The true velocity profile is indicated by the red dotted line.

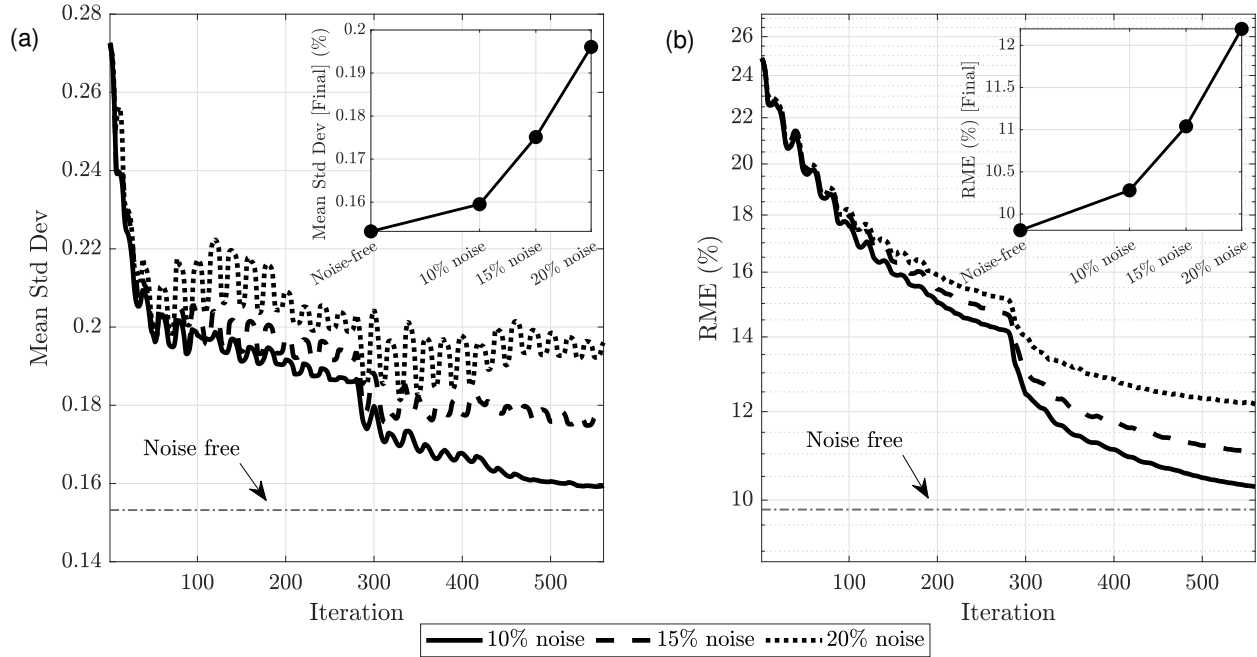


Figure 22: Convergence behavior of the Marmoussi II inversion for different noise levels. (a) Mean pointwise posterior standard deviation versus iteration number. (b) Relative model error versus iteration number. Higher noise levels result in increased uncertainty and larger model errors throughout the inversion process.

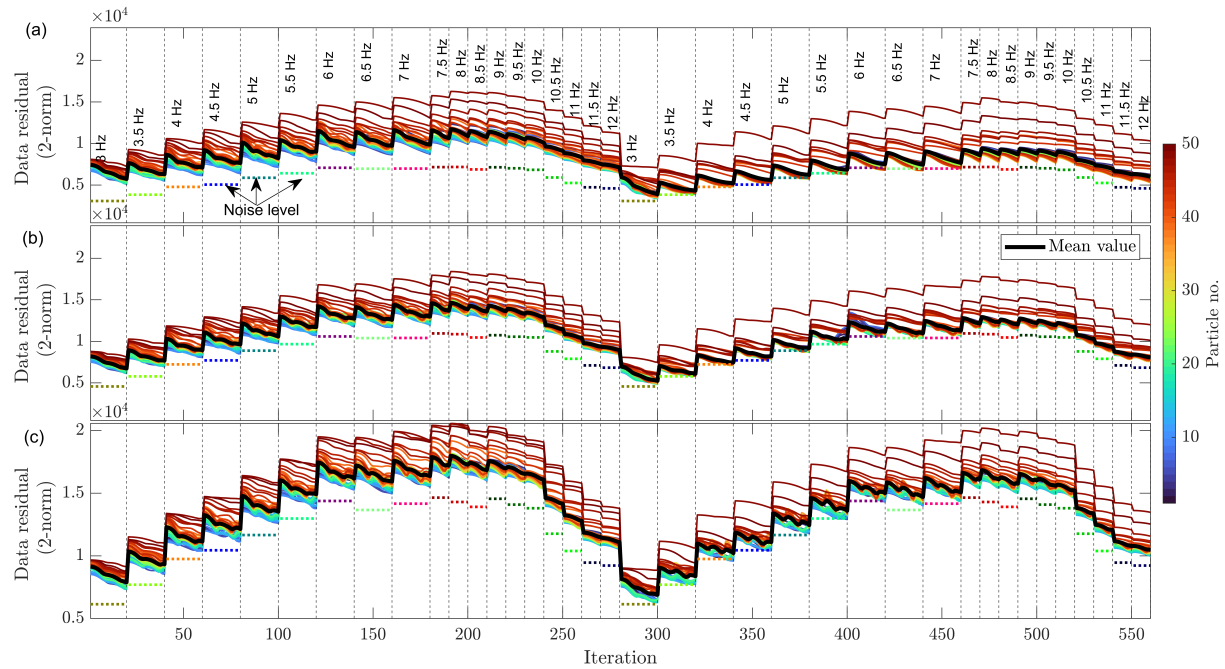


Figure 23: Per-particle data residual (2-norm) as a function of iteration number across two inversion cycles for (a) 10%, (b) 15%, and (c) 20% noise levels. Each colored line corresponds to an individual particle, with the color encoding the particle index as indicated by the colorbar. The black solid line denotes the ensemble mean residual. Vertical dashed lines mark frequency transitions within each cycle, with the corresponding frequency label annotated at the top of panel (a). The horizontal dotted lines indicate the noise level for each frequency, with colors matched to the frequency labels.

Large values of  $\mu$  enforce the constraint rapidly but can make the augmented posterior too narrow in early iterations, potentially trapping particles in local modes. Small values slow convergence but allow broader exploration. As discussed in Section 6.4, the compound parameter  $\mu\sigma^2$  is adaptively determined at each iteration using the residual whiteness principle [42], which removes the need for manual tuning and provides a robust balance between constraint enforcement and posterior exploration in all of our experiments.

As observed in the Rosenbrock example, deterministic particle methods like SVGD can struggle with multimodal posteriors when modes are separated by low-probability regions. The SVGD kernel repulsion maintains local diversity but cannot transport particles across distant modes once they have settled. This is an inherent limitation of deterministic transport methods compared to stochastic samplers such as MCMC [28, 5, 9]. The comparison with standard SVGD on the Rosenbrock example confirms that, for this low-dimensional problem, both SVGD variants produce comparable posterior approximations. However, the ADMM splitting is expected to yield significant conditioning advantages for higher-dimensional constrained problems such as FWI, where the tight coupling between model and wavefield variables makes the reduced-space posterior landscape substantially more ill-conditioned. For the FWI examples, where the posterior is expected to be more concentrated, the mode-crossing limitation did not noticeably affect the results. In applications where strong multimodality is anticipated, combining ADMM-SVGD with stochastic perturbations or tempering schemes may be beneficial.

The Marmousi II experiment demonstrates that ADMM-SVGD can be applied to models with realistic complexity. The memory cost scales linearly with  $N_p$ , as each particle maintains its own set of auxiliary variables and multipliers. The number of particles must be chosen large enough to adequately represent the posterior—too few particles leads to underestimation of the posterior spread due to SVGD’s mode-seeking behavior [34], as also observed in the frugal SVGD-based FWI framework of Izzatullah et al. [57]. A systematic study of the particle count versus posterior calibration for large-scale FWI applications is an interesting avenue for future work. Alternatively, neural control variates based on Stein’s identity [58] could reduce the variance of posterior expectations computed from the particle ensemble, partially mitigating the effect of using a limited number of particles. Recent work on 3-D Bayesian variational FWI using stochastic SVGD [59] provides promising directions for scaling particle-based methods to larger problems.

The closest related work is that of Fang et al. [17], who share our starting point of relaxing the PDE constraint for Bayesian inference. The key difference is that their Gaussian approximation centered at the MAP estimate [18] is limited to unimodal posteriors, whereas our particle-based approach captures arbitrary posterior geometries, including the multimodality observed on Marmousi II. Additionally, our ADMM multiplier updates progressively enforce the constraint without requiring careful a priori calibration of the penalty parameter. The split-and-augmented Gibbs sampler of Vono et al. [50] uses a similar ADMM-type splitting but relies on exact conditional sampling; their dimension-free convergence analysis [51] provides indirect theoretical support for our approach. More broadly, ADMM-SVGD connects to the growing body of work bridging optimization and sampling [60, 61, 62] and on Stein methods for geophysical inference [34, 35]. Alternative approaches to Bayesian inference in seismic problems [63, 64] include deep-learning based methods [65, 66, 67, 68, 69], amortized variational inference with normalizing flows [70, 71, 20, 72], and transport-map accelerated sampling [73]. The augmented Lagrangian formulation has also been extended to time-domain FWI [14], dual formulations [40, 12], time-lapse monitoring [74], and differentiable programming frameworks [75].

Several directions remain for future work. First, preconditioning the SVGD updates with matrix-valued kernels [76] or projected Newton directions [77] could reduce the number of particles and iterations needed, alleviating the linear cost scaling with ensemble size. Second, extending the formulation to time-domain FWI—where broadband data can be processed in a single solve rather than sweeping over discrete frequencies—would reduce the number of outer iterations. Third, replacing the particle ensemble with normalizing-flow posteriors or neural-network-based priors could amortize the sampling cost, providing instant posterior samples for new data without iterative updates.

## 9 Conclusion

We have presented ADMM-SVGD, a method for posterior sampling in constrained inverse problems that combines the alternating direction method of multipliers with Stein variational gradient descent. By exploiting the probabilistic interpretation of the augmented Lagrangian, the method translates hard PDE constraints into a sequence of evolving target distributions that are amenable to particle-based sampling, while the ADMM multiplier updates ensure that the constraints are progressively enforced. This dual-space approach inherits the favorable conditioning properties of wavefield reconstruction inversion while enabling principled uncertainty quantification through the SVGD particle ensemble.

Numerical experiments on the Rosenbrock distribution validated the method against standard SVGD as a baseline without constraint splitting, confirming well-calibrated posteriors with accurate coverage of the true parameter values.

Application to frequency-domain full waveform inversion—for both a Gaussian anomaly model and the Marmousi II benchmark—demonstrated that the method produces physically meaningful uncertainty estimates: credible intervals that contain the true model, pointwise standard deviations that are spatially correlated with estimation error, and posterior contraction with increasing data coverage. On the Marmousi II model, the method revealed multimodal posterior structure at geologically complex locations, highlighting the value of full posterior characterization over single-point estimates.

## Acknowledgments

Ali Siahkoochi acknowledges support from the Institute for Artificial Intelligence at the University of Central Florida.

## References

- [1] Jean Virieux and Stéphane Operto. An overview of full-waveform inversion in exploration geophysics. *Geophysics*, 74(6):WCC1–WCC26, 2009.
- [2] Albert Tarantola. *Inverse Problem Theory and Methods for Model Parameter Estimation*. SIAM, 2005.
- [3] Andrew M. Stuart. Inverse problems: a Bayesian perspective. *Acta Numerica*, 19:451–559, 2010.
- [4] Andrew Curtis and Anthony Lomax. Prior information, sampling distributions, and the curse of dimensionality. *Geophysics*, 66(2):372–378, 2001.
- [5] James Martin, Lucas C. Wilcox, Carsten Burstedde, and Omar Ghattas. A stochastic Newton MCMC method for large-scale statistical inverse problems with application to seismic inversion. *SIAM Journal on Scientific Computing*, 34(3):A1460–A1487, 2012.
- [6] Andreas Fichtner and Saulè Simutè. Hamiltonian Monte Carlo inversion of seismic sources in complex media. *Journal of Geophysical Research: Solid Earth*, 123(4):2984–2999, 2018.
- [7] Anandaroop Ray, Sam Kaplan, John Washbourne, and Uwe Albertin. Low frequency full waveform seismic inversion within a tree based Bayesian framework. *Geophysical Journal International*, 212(1):522–542, 2017.
- [8] Gregory Ely, Alison Malcolm, and Oleg V. Poliannikov. Assessing uncertainties in velocity models and images with a fast nonlinear uncertainty quantification method. *Geophysics*, 83(2):R63–R75, 2018.
- [9] Zeyu Zhao and Mrinal K. Sen. A gradient-based Markov chain Monte Carlo method for full-waveform inversion and uncertainty analysis. *Geophysics*, 86(1):R15–R30, 2021.
- [10] Tristan van Leeuwen and Felix J. Herrmann. Mitigating local minima in full-waveform inversion by expanding the search space. *Geophysical Journal International*, 195(1):661–667, 2013.
- [11] Tristan van Leeuwen and Felix J. Herrmann. A penalty method for PDE-constrained optimization in inverse problems. *Inverse Problems*, 32(1):015007, 2016.
- [12] Gabrio Rizzuti, Mathias Louboutin, Rongrong Wang, and Felix J. Herrmann. A dual formulation of wavefield reconstruction inversion for large-scale seismic inversion. *Geophysics*, 86(6):R879–R893, 2021.
- [13] Hossein S. Aghamiry, Ali Gholami, and Stéphane Operto. Improving full-waveform inversion by wavefield reconstruction with the alternating direction method of multipliers. *Geophysics*, 84(1):R139–R162, 2019.
- [14] Ali Gholami, Hossein S. Aghamiry, and Stéphane Operto. Extended-space full-waveform inversion in the time domain with the augmented Lagrangian method. *Geophysics*, 87(1):R63–R77, 2022.
- [15] Stéphane Operto, Ali Gholami, Hossein S. Aghamiry, Gaoshan Guo, Stephen Beller, Kamal Aghazade, Fricnel Mamfoumbi, Laure Combe, and Alessandra Ribodetti. Extending the search space of full-waveform inversion beyond the single-scattering Born approximation: A tutorial review. *Geophysics*, 88(6):R671–R702, 2023.
- [16] Michael Fisher, Martin Leutbecher, and Gavin Kelly. On the equivalence between Kalman smoothing and weak-constraint four-dimensional variational data assimilation. *Quarterly Journal of the Royal Meteorological Society*, 131:3235–3246, 2005.
- [17] Zhilong Fang, Curt Da Silva, Rachel Kuske, and Felix J. Herrmann. Uncertainty quantification for inverse problems with weak partial-differential-equation constraints. *Geophysics*, 83(6):R629–R647, 2018.
- [18] Johnathan M. Bardsley, Antti Solonen, Heikki Haario, and Marko Laine. Randomize-then-optimize: a method for sampling from posterior distributions in nonlinear inverse problems. *SIAM Journal on Scientific Computing*, 36(4):A1895–A1910, 2014.

- [19] W. K. Hastings. Monte Carlo sampling methods using Markov chains and their applications. *Biometrika*, 57(1): 97–109, 1970.
- [20] Ali Siahkoohi, Gabrio Rizzuti, Rafael Orozco, and Felix J. Herrmann. Reliable amortized variational inference with physics-based latent distribution correction. *Geophysics*, 88(3):R297–R322, 2023.
- [21] Ziyi Yin, Rafael Orozco, and Felix J. Herrmann. WISER: Multimodal variational inference for full-waveform inversion without dimensionality reduction. *Geophysics*, 90(2):A1–A7, 2025.
- [22] Xuebin Zhao and Andrew Curtis. Physically structured variational inference for Bayesian full waveform inversion. *Journal of Geophysical Research: Solid Earth*, 129(11):e2024JB029557, 2024.
- [23] Xuebin Zhao and Andrew Curtis. Efficient Bayesian full-waveform inversion and analysis of prior hypotheses in three dimensions. *Geophysics*, 90(6):R373–R388, 2025.
- [24] Richard C. Aster, Brian Borchers, and Clifford H. Thurber. *Parameter Estimation and Inverse Problems*. Elsevier, 2018. doi: 10.1016/C2015-0-02458-3.
- [25] Jari Kaipio and Erkki Somersalo. *Statistical and Computational Inverse Problems*. Springer, 2005.
- [26] Alberto Malinverno and Victoria A. Briggs. Expanded uncertainty quantification in inverse problems: Hierarchical Bayes and empirical Bayes. *Geophysics*, 69(4):1005–1016, 2004.
- [27] Christian P. Robert and George Casella. *Monte Carlo Statistical Methods*. Springer-Verlag, 2004.
- [28] Klaus Mosegaard and Albert Tarantola. Monte Carlo sampling of solutions to inverse problems. *Journal of Geophysical Research: Solid Earth*, 100(B7):12431–12447, 1995.
- [29] Brian D. O. Anderson and John B. Moore. *Optimal Filtering*. Prentice-Hall, Englewood Cliffs, NJ, 1979.
- [30] David J. C. MacKay. *Information Theory, Inference and Learning Algorithms*. Cambridge University Press, 2003.
- [31] Ali Siahkoohi, Gabrio Rizzuti, and Felix J. Herrmann. A deep-learning based Bayesian approach to seismic imaging and uncertainty quantification. In *82nd EAGE Conference and Exhibition, Extended Abstracts*, 2020. doi: 10.3997/2214-4609.202010770.
- [32] Ali Siahkoohi, Gabrio Rizzuti, and Felix J. Herrmann. Uncertainty quantification in imaging and automatic horizon tracking—a Bayesian deep-prior based approach. In *90th Annual International Meeting, SEG, Expanded Abstracts*, pages 1636–1640, 2020. doi: 10.1190/segam2020-3417560.1.
- [33] Ali Siahkoohi, Gabrio Rizzuti, and Felix J. Herrmann. Weak deep priors for seismic imaging. In *90th Annual International Meeting, SEG, Expanded Abstracts*, pages 2998–3002, 2020. doi: 10.1190/segam2020-3417568.1.
- [34] Qiang Liu and Dilin Wang. Stein variational gradient descent: a general purpose Bayesian inference algorithm. In *Advances in Neural Information Processing Systems*, 2016.
- [35] Xin Zhang and Andrew Curtis. Variational full-waveform inversion. *Geophysical Journal International*, 222(1): 406–411, 2020.
- [36] Miguel Corrales, Sean Berti, Bertrand Denel, Paul Williamson, Mattia Aleardi, and Matteo Ravasi. Annealed Stein variational gradient descent for improved uncertainty estimation in full-waveform inversion. *Geophysical Journal International*, 241(2):1088–1113, 2025.
- [37] R.-E. Plessix. A review of the adjoint-state method for computing the gradient of a functional with geophysical applications. *Geophysical Journal International*, 167(2):495–503, 2006.
- [38] R. Gerhard Pratt. Seismic waveform inversion in the frequency domain, Part 1: Theory and verification in a physical scale model. *Geophysics*, 64(3):888–901, 1999.
- [39] Eldad Haber, Uri M. Ascher, and Doug Oldenburg. On optimization techniques for solving nonlinear inverse problems. *Inverse problems*, 16(5):1263–1280, 2000.
- [40] Kamyar Aghazade and Ali Gholami. Fast and automatic full waveform inversion by dual augmented Lagrangian. *Computational Geosciences*, 29(4):34, 2025.
- [41] Ernie Esser, Lluís Guasch, Tristan van Leeuwen, Aleksandr Y. Aravkin, and Felix J. Herrmann. Total variation regularization strategies in full-waveform inversion. *SIAM Journal on Imaging Sciences*, 11(1):376–406, 2018.
- [42] Kamal Aghazade, Toktam Zand, and Ali Gholami. Automatic Penalty Parameter Selection by Residual Whiteness Principle (RWP) and GCV for Full Waveform Inversion. *arXiv preprint arXiv:2512.16757*, 2025.
- [43] Toktam Zand, Hamid R. Siahkoohi, Alison Malcolm, Ali Gholami, and Alan Richardson. Consensus optimization of total variation-based reverse time migration. *Computational Geosciences*, 24(3):1393–1407, 2020. doi: 10.1007/s10596-020-09958-1.

- [44] Richard A. Tapia. Diagonalized multiplier methods and quasi-Newton methods for constrained optimization. *Journal of Optimization Theory and Applications*, 22(2):135–194, 1977. doi: 10.1007/BF00933161.
- [45] Angelo Miele, Philip E. Moseley, Allen V. Levy, and George M. Coggins. On the method of multipliers for mathematical programming problems. *Journal of Optimization Theory and Applications*, 10(1):1–33, 1972. doi: 10.1007/BF00934960.
- [46] Jonathan Eckstein and Dimitri P. Bertsekas. On the Douglas–Rachford splitting method and the proximal point algorithm for maximal monotone operators. *Mathematical Programming*, 55:293–318, 1992.
- [47] Stephen Boyd, Neal Parikh, Eric Chu, Borja Peleato, and Jonathan Eckstein. Distributed optimization and statistical learning via the alternating direction method of multipliers. *Foundations and Trends in Machine Learning*, 3(1):1–122, 2011.
- [48] Mingyi Hong, Zhi-Quan Luo, and Meisam Razaviyayn. Convergence analysis of alternating direction method of multipliers for a family of nonconvex problems. *SIAM Journal on Optimization*, 26(1):337–364, 2016.
- [49] Yu Wang, Wotao Yin, and Jinshan Zeng. Global convergence of ADMM in nonconvex nonsmooth optimization. *Journal of Scientific Computing*, 78:29–63, 2019.
- [50] Maxime Vono, Nicolas Dobigeon, and Pierre Chainais. Split-and-augmented Gibbs sampler—application to large-scale inference problems. *IEEE Transactions on Signal Processing*, 67(6):1648–1661, 2019.
- [51] Maxime Vono, Daniel Paulin, and Arnaud Doucet. Efficient MCMC sampling with dimension-free convergence rate using ADMM-type splitting. *Journal of Machine Learning Research*, 23(25):1–69, 2022.
- [52] Anna Korba, Adil Salim, Michael Arbel, Giulia Luise, and Arthur Gretton. A non-asymptotic analysis for Stein variational gradient descent. In *Advances in Neural Information Processing Systems*, 2020.
- [53] Carl Edward Rasmussen and Christopher K. I. Williams. *Gaussian Processes for Machine Learning*. MIT Press, 2006.
- [54] Xuebin Zhao and Andrew Curtis. Variational prior replacement in Bayesian inference and inversion. *Geophysical Journal International*, 239(2):1236–1256, 2024.
- [55] Carey Bunks, Fatimetou M. Saleck, Stephane Zaleski, and Guy Chavent. Multiscale seismic waveform inversion. *Geophysics*, 60(5):1457–1473, 1995.
- [56] Gary S. Martin, Robert Wiley, and Kurt J. Marfurt. Marmousi2: An elastic upgrade for Marmousi. *The Leading Edge*, 25(2):156–166, 2006.
- [57] Muhammad Izzatullah, Abdullah Alali, Matteo Ravasi, and Tariq Alkhalifah. Physics-reliable frugal local uncertainty analysis for full waveform inversion. *Geophysical Prospecting*, 72(7):2718–2738, 2024. doi: <https://doi.org/10.1111/1365-2478.13528>.
- [58] Ali Siahkoohi and Hyunwoo Oh. Conditional neural control variates for variance reduction in Bayesian inverse problems. *arXiv preprint arXiv:2602.21357*, 2026.
- [59] Xin Zhang, Angus Lomas, Muhong Zhou, York Zheng, and Andrew Curtis. 3-D Bayesian variational full waveform inversion. *Geophysical Journal International*, 234(1):546–561, 2023.
- [60] Michael I. Jordan, Zoubin Ghahramani, Tommi S. Jaakkola, and Lawrence K. Saul. An introduction to variational methods for graphical models. *Machine Learning*, 37(2):183–233, 1999.
- [61] David M. Blei, Alp Kucukelbir, and Jon D. McAuliffe. Variational inference: a review for statisticians. *Journal of the American Statistical Association*, 112(518):859–877, 2017.
- [62] Nicolás García Trillos, Bamdad Hosseini, and Daniel Sanz-Alonso. From optimization to sampling through gradient flows. *Notices of the American Mathematical Society*, 70(6):905–917, 2023.
- [63] Tan Bui-Thanh, Omar Ghattas, James Martin, and Georg Stadler. A computational framework for infinite-dimensional Bayesian inverse problems part I: The linearized case, with application to global seismic inversion. *SIAM Journal on Scientific Computing*, 35(6):A2494–A2523, 2013.
- [64] Hejun Zhu, Siwei Li, Sergey Fomel, Georg Stadler, and Omar Ghattas. A Bayesian approach to estimate uncertainty for full-waveform inversion using a priori information from depth migration. *Geophysics*, 81(5):R307–R323, 2016.
- [65] Jonas Adler and Ozan Öktem. Deep Bayesian inversion. *arXiv preprint arXiv:1811.05910*, 2018.
- [66] Ali Siahkoohi, Gabrio Rizzuti, and Felix J. Herrmann. Deep Bayesian inference for seismic imaging with tasks. *Geophysics*, 87(5):S281–S302, 2022.

- [67] Lorenzo Baldassari, Ali Siahkoohi, Josselin Garnier, Knut Sølna, and Maarten V. de Hoop. Conditional score-based diffusion models for Bayesian inference in infinite dimensions. In *Advances in Neural Information Processing Systems*, volume 36, pages 24262–24290, 2023.
- [68] Lingyun Yang, Omar M. Saad, Guochen Wu, and Tariq Alkhalifah. Conditional image prior for uncertainty quantification in full-waveform inversion. In *SEG/AAPG International Meeting for Applied Geoscience & Energy*, pages SEG–2024–4090025, 2024. doi: 10.1190/image2024-4090025.1.
- [69] Yunlin Zeng, Huseyin Tuna Erdinc, Rafael Orozco, and Felix Herrmann. Full-waveform variational inference with full common-image gathers and diffusion network. *arXiv preprint arXiv:2504.15289*, 2025.
- [70] Danilo Rezende and Shakir Mohamed. Variational inference with normalizing flows. In *Proceedings of the 32nd International Conference on Machine Learning*, volume 37, pages 1530–1538, 2015.
- [71] Stefan T. Radev, Ulf K. Mertens, Andreas Voss, Lynton Ardizzone, and Ullrich Köthe. BayesFlow: Learning complex stochastic models with invertible neural networks. *IEEE Transactions on Neural Networks and Learning Systems*, 33:1452–1466, 2022.
- [72] Rafael Orozco, Ali Siahkoohi, Mathias Louboutin, and Felix J. Herrmann. ASPIRE: Iterative amortized posterior inference for Bayesian inverse problems. *Inverse Problems*, 41(4):045001, 2025.
- [73] Matthew D. Parno and Youssef M. Marzouk. Transport map accelerated Markov chain Monte Carlo. *SIAM/ASA Journal on Uncertainty Quantification*, 6(2):645–682, 2018.
- [74] Xin Zhang and Andrew Curtis. Bayesian variational time-lapse full waveform inversion. *Geophysical Journal International*, 237(3):1624–1638, 2024.
- [75] Mathias Louboutin, Ziyi Yin, Rafael Orozco, Thomas J. Grady II, Ali Siahkoohi, Gabrio Rizzuti, Philipp A. Witte, Olav Møyner, Gerard J. Gorman, and Felix J. Herrmann. Learned multiphysics inversion with differentiable programming and machine learning. *The Leading Edge*, 42(7):474–486, 2023.
- [76] Dilin Wang, Ziyang Tang, Chandrajit Bajaj, and Qiang Liu. Stein variational gradient descent with matrix-valued kernels. In *Advances in Neural Information Processing Systems*, volume 32, pages 7834–7844, 2019.
- [77] Peng Chen, Keyi Wu, Joshua Chen, Tom O’Leary-Roseberry, and Omar Ghattas. Projected Stein variational Newton: a fast and scalable Bayesian inference method in high dimensions. In *Advances in Neural Information Processing Systems*, volume 32, pages 15104–15113, 2019.